High precision ringdown modeling: Multimode fits and BMS frames

Lorena Magaña Zertuche, Keefe Mitman, Neev Khera, Leo C. Stein, Michael Boyle, Nils Deppe, François Hébert, Dante A. B. Iozzo, Lawrence E. Kidder, Jordan Moxon, Harald P. Pfeiffer, Mark A. Scheel, Saul A. Teukolsky, William Throwe, and Nils Vu

High Precision Ringdown Modeling: Multimode Fits and BMS Frames

Lorena Magaña Zertuche [iD],[1, *] Keefe Mitman [iD],[2, †] Neev Khera [iD],[3, ‡] Leo C. Stein [iD],[1, §]
Michael Boyle [iD],[4] Nils Deppe [iD],[2] François Hébert [iD],[2] Dante A. B. Iozzo [iD],[4] Lawrence E. Kidder [iD],[4] Jordan
Moxon [iD],[2] Harald P. Pfeiffer [iD],[5] Mark A. Scheel [iD],[2] Saul A. Teukolsky [iD],[2, 4] William Throwe [iD],[4] and Nils Vu [iD][5]

[1] *Department of Physics and Astronomy, University of Mississippi, University, Mississippi 38677, USA*
[2] *Theoretical Astrophysics 350-17, California Institute of Technology, Pasadena, California 91125, USA*
[3] *Institute for Gravitation and the Cosmos & Physics Department, Penn State, University Park, Pennsylvania 16802, USA*
[4] *Cornell Center for Astrophysics and Planetary Science, Cornell University, Ithaca, New York 14853, USA*
[5] *Max Planck Institute for Gravitational Physics (Albert Einstein Institute), Am Mühlenberg 1, Potsdam 14476, Germany*
(Dated: March 11, 2022)

Quasi-normal mode (QNM) modeling is an invaluable tool for characterizing remnant black holes, studying strong gravity, and testing general relativity. Only recently have QNM studies begun to focus on multimode fitting to numerical relativity strain waveforms. As gravitational wave observatories become even more sensitive they will be able to resolve higher-order modes. Consequently, multimode QNM fits will be critically important, and in turn require a more thorough treatment of the asymptotic frame at $\mathscr{I}^+$. The first main result of this work is a method for systematically fitting a QNM model containing many modes to a numerical waveform produced using Cauchy-characteristic extraction (CCE), a waveform extraction technique which is known to resolve memory effects. We choose the modes to model based on their power contribution to the residual between numerical and model waveforms. We show that the all-mode strain mismatch improves by a factor of $\sim 10^5$ when using multimode fitting as opposed to only fitting the $(2, \pm 2, n)$ modes. Our most significant result addresses a critical point that has been overlooked in the QNM literature: the importance of matching the Bondi-van der Burg-Metzner-Sachs (BMS) frame of the numerical waveform to that of the QNM model. We show that by mapping the numerical waveforms—which exhibit the memory effect—to a BMS frame known as the super rest frame, there is an improvement of $\sim 10^5$ in the all-mode strain mismatch compared to using a strain waveform whose BMS frame is not fixed. Furthermore, we find that by mapping CCE waveforms to the super rest frame, we can obtain all-mode mismatches that are, on average, a factor of ~ 4 better than using the publicly-available extrapolated waveforms. We illustrate the effectiveness of these modeling enhancements by applying them to families of waveforms produced by numerical relativity and comparing our results to previous QNM studies.

I. INTRODUCTION

When in a vacuum a black hole can be considered one of the simplest objects in the universe, since it is fully characterized by its mass and angular momentum. Despite this simplicity, black holes continue to be challenging to study with a multitude of important and unanswered questions concerning them [1]. Currently, a rather promising means of studying black holes is through gravitational wave astronomy, i.e., using observations of gravitational waves emitted by binary black hole (BBH), black hole-neutron star (BH-NS), and possibly binary neutron star (BNS) mergers to study properties of the perturbed remnant black holes [2–5]. While the waveform that is emitted during the merger phase is challenging to model and requires the aid of numerical simulations [6–10], the radiation emitted by the remnant black hole during its ringdown phase is expected to oscillate at a certain set of well-understood frequencies, called quasi-normal mode

(QNM) frequencies, until the remnant black hole settles into a final state of equilibrium [11].

Fortunately, these QNM frequencies can be computed using perturbation theory and are completely determined by the remnant's mass and spin, thereby allowing for a thorough analysis of the remnant black hole's properties, provided the QNM model is used properly when fitting to the observed gravitational waves [12–16]. Often, these QNMs are labeled by the numbers $\{\ell, m, n\}$, where (ℓ, m) are the angular numbers that correspond to spin-weighted spheroidal harmonics (see [17]) and $n = 0, 1, \ldots$ is the overtone number that sorts the QNM frequencies in order of decreasing damping timescales, with the fundamental $n = 0$ mode being the least-damped mode.

Recently, gravitational wave analysis efforts have shifted their focus from modes with $\ell = 2$, $m = 2$ to multiple (ℓ, m) modes through studies that explore the effects of overtones, retrograde modes, and mode-mixing [18–26].[1] Moreover, third-generation, ground-based detectors such as the Einstein Telescope (ET) and Cosmic Explorer (CE)

* lmaganaz@go.olemiss.edu
† kmitman@caltech.edu
‡ neevkhera@psu.edu
§ lcstein@olemiss.edu

[1] By mode-mixing effects, we mean the mixing that occurs when writing a QNM model in a spherical harmonic basis, rather than its preferred spheroidal harmonic basis.

are expected to observe roughly $10^2 - 10^4$ events per year with ringdown signals that will be strong enough to exhibit various higher-order mode contributions, which, until now, have not been systematically studied [27, 28]. Consequently, being able to include higher-order modes in QNM models is vitally important for future analyses, since this will be essential for ensuring that the dynamics of the observed remnant black holes are accurately captured and measured. In addition, the Laser Interferometer Space Antenna (LISA) will be even more sensitive to the ringdown phase of compact mergers, thereby allowing for even more inclusive multi-frequency ringdown studies that may aid with black hole astronomy and testing various theories of relativity [29–31].

Apart from the clear importance of including overtones, retrograde modes, mode-mixing effects, and higher-order modes in analyses of gravitational waves that are emitted during ringdown [18–26], there is one other crucial component to QNM modeling that is absent in prior QNM studies: ensuring that the waveforms and the QNM model are in identical Bondi-van der Burg-Metzner-Sachs (BMS) frames. Until now, studies that have compared numerical relativity (NR) waveforms to QNMs have not considered the frame of their waveforms during the ringdown phase. While many of them have used NR waveforms whose inspiral phase has been mapped to the center-of-mass frame [7, 32],[2] this is very different from mapping the ringdown phase to a certain frame, such as the center-of-mass frame of the remnant BH. Nonetheless, even if one were to map the remnant to the center-of-mass frame, rather than the inspiraling BHs, this procedure would still be lacking due to a subtle, but important feature of relativity. Namely, the fact that for asymptotically flat spacetimes the symmetry group of future null infinity $\mathscr{I}^+$ is not the Poincaré group, but the infinite-dimensional BMS group [34, 35].

Fundamentally, the BMS group is just an extension of the Poincaré group, in which spacetime translations are replaced by an encompassing collection of transformations known as *supertranslations*. When working with Bondi coordinates $(u \equiv t - r, r, \theta, \phi)$, these supertranslations can be understood rather simply as being direction-dependent time translations. Namely, a supertranslation transforms the time coordinate via $u \rightarrow u - \alpha(\theta, \phi)$, with α being an arbitrary function. Therefore, when fitting QNMs to a waveform, one not only needs to map to the center-of-mass frame with the remnant BH's spin aligned with the positive z-axis, i.e., fixing the Poincaré frame, but they also need to fix the supertranslation freedom of their waveforms to ensure that comparisons with QNMs are meaningful. Using an incorrect BMS frame leads to two effects that are sources of errors in the fits: the waveform is shifted and settles down to a nonzero value, and there is a mixing of modes that is distinct from the spherical-spheroidal mixing mentioned before [33, 36].

Across this work, we perform QNM fits by including every one of the important aforementioned components to modeling NR ringdowns with QNMs, i.e., overtones, retrograde modes, mode-mixing, higher-order modes, and BMS frame fixing. More specifically, we simultaneously fit various modes over all angles on the two-sphere while also accounting for the mode-mixing that occurs because NR waveforms are in a spherical harmonic basis, while our QNM model is in a spheroidal harmonic basis. When trying to model such a large number of modes and their overtones, we must choose which modes to model. We do this systematically by examining which modes in our model contain the largest portion of unmodeled power (see Sec. III for more detail). Apart from this, we also map our NR waveforms to the BMS frame that is expected by the QNM model, namely, the super rest frame (see Sec. II B for more detail) [33, 37–39].[3] We, therefore, create a QNM model by choosing modes based on their unmodeled power and, for the first time, fit said model to a NR waveform that has been properly mapped to the same BMS frame as is expected by the Teukolsky formalism [11]. We find that by carrying out this procedure, i.e., fitting over the whole two-sphere and accounting for BMS frames, we can drastically enhance previous results, such as the GW150914 investigations in Giesler et al. [18] and Cook [19], by both reducing mismatches between NR waveforms and QNM models by a factor of 10^5 as well as improving parameter estimates of the remnant black hole's characteristics by more than half an order of magnitude using QNMs. We tested the effects of multimode modeling and frame fixing with 14 SXS simulations (see Table I), which include systems of mass ratio 1 and 4, with varying spin configurations, including precessions. We also provide an in-depth study on the simulation SXS:BBH:0305, a proxy for GW150914.

We present our computations and results as follows. In Sec. II, we outline the mathematical conventions for waveform modeling that is used throughout the paper. Furthermore, we also discuss the reason why fixing the BMS frame is important and present how we will map our waveforms to the super rest frame. Next, in Sec. III, we discuss our greedy algorithm for choosing modes to include in our QNM model and highlight the importance of multimode fitting for ringdown modeling. We also show how multimode fitting affects the mismatch between a NR waveform and a QNM model. Finally, in Sec. IV we show the importance of mapping the remnant black hole to the super rest frame and the consequences of using the correct BMS frame when fitting to QNMs.

---

[2] See [33] for an improved way to map to the center-of-mass frame.

---

[3] Note that in this work when we refer to mapping a waveform to the super rest frame we really mean simultaneously mapping to the remnant BH's center-of-mass frame, aligning the remnant BH's spin with the positive z-axis, and fixing the supertranslation freedom by mapping to the super rest frame of [33].

II. FORMALISM

The remnant black hole formed from a BBH merger is well-described as a supertranslated Kerr metric with (potentially large) perturbations, which decay with time. As shown by Teukolsky in 1973 [11], applying perturbation theory to the Kerr spacetime, one acquires a decoupled "master equation" that describes linear curvature perturbations of the black hole. The Teukolsky partial differential equation also separates into temporal, radial, and angular ordinary differential equations. The oscillatory yet exponentially decaying modal solutions are the QNMs, and the spacetime after merger is modeled as a linear superposition of many of these QNMs. Imposing appropriate conditions of decay (at null infinity, $\mathscr{I}$) and regularity (at the horizon and poles) quantizes the allowed complex QNM frequencies [13]. One finds the frequencies, separation constants, and angular wavefunctions simultaneously, either via Leaver's original approach of infinite continued fractions [13], or a more recent spectral eigenvalue approach of Cook and Zalutskiy [15, 19]. The spectral approach finds the angular mode shapes—the spin-weighted spheroidal harmonics—as a decomposition in spin-weighted spherical harmonics. This decomposition has been employed before in [19, 20, 22, 25, 26, 40]. We obtain the QNM frequencies and spherical-spheroidal decomposition coefficients from the open-source Python package `qnm`, which uses a Leaver solver for the radial sector, with the spectral eigenvalue approach for the angular sector [13, 41]. For more details on the implementation see [41] and references therein.

In this study, we are exclusively interested in working with complex waveforms, like the strain h,[4] which are decomposed into spin-weight -2 spherical harmonic bases and live on future null infinity $\mathscr{I}^+$. We write these waveforms as, e.g.,

$$h(u, \theta, \phi) = \sum_{\ell \geq 2, |m| \leq \ell} h_{\ell m}(u) \, _{-2}Y_{\ell m}(\theta, \phi). \qquad (1)$$

The spin-weighted spherical harmonics of fixed spin-weight s form a complete and orthonormal basis on the two-sphere [42, 43],

$$\int_{S^2} (_sY_{\ell m})^* \, _sY_{\ell' m'} \, d\Omega = \delta_{\ell \ell'} \delta_{mm'}, \qquad (2)$$

where $*$ denotes complex conjugation and the differential $d\Omega = d\cos\theta \, d\phi$ is the standard volume element on the two-sphere.

A. QNM formalism

For a given black hole spin $|a| < M$, and choice of angular numbers (ℓ, m), there are an infinite number of QNM

---

[4] We explicitly define the strain as described in Appendix C of [7].

Ordinary/mirror/prograde/retrograde QNM frequencies ($a = 0.7M$)
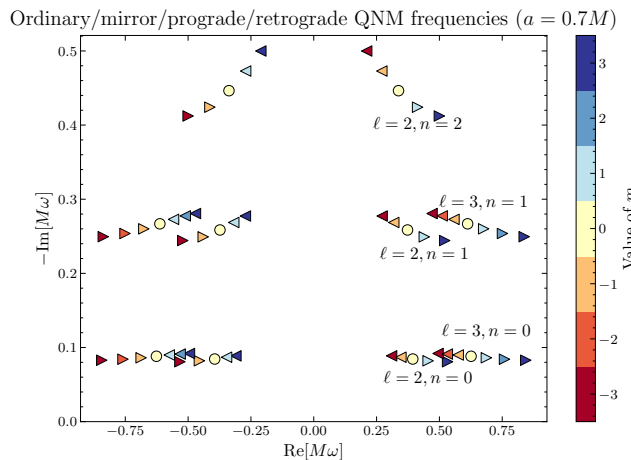

FIG. 1. Right-pointing triangles are prograde modes, left-pointing triangles are retrograde. Note that prograde and retrograde modes are present both in the left half-plane (so-called "mirror" modes) and the right half-plane (ordinary modes).

frequencies satisfying the boundary conditions. These are all in the lower half-plane, $\text{Im}[\omega] < 0$, as required by stability. The symmetry of the equations means that if $\omega_{\ell m}$ is a QNM frequency, then so is $-\omega_{\ell,-m}^*$; this is a "mirror" symmetry between the left and right half-planes. This leads to the nomenclature (see also Table I of [26])

- "ordinary" mode: $\text{Re}[\omega] > 0$,

- "mirror" mode: $\text{Re}[\omega] < 0$.

Because of this symmetry, much of the QNM literature has focused on just the ordinary modes, since the mirror modes can be recovered via the transformation $\{m \to -m, \omega \to -\omega^*\}$. Within each family, there are still an infinite number of overtones. Thus to uniquely identify each solution, we label the mode $\omega_{\ell m n}^p$ with $\{\ell, m, n, p\}$, where $n = 0, 1, \ldots$ is the overtone number, ordered by the magnitude of $\text{Im}[\omega]$, and $p = \text{sgn}(\text{Re}[\omega])$ is either ± 1. The least-damped $n = 0$ mode is often called the fundamental mode or zeroth tone while the $n > 0$ modes are referred to as overtones [16].

Moreover, there are prograde and retrograde modes in both the right and left (mirror) half-planes [16, 26, 40, 44]. A QNM is labeled prograde if its wavefronts circulate around the BH in the same sense as its rotation. Because a QNM solution goes as $\propto \exp(-i\omega t + im\phi)$, we see that surfaces of constant phase circulate in the positive ϕ direction when

- "prograde" mode: $\text{sgn}(m) = +\text{sgn}(\text{Re}[\omega])$,

and in the negative ϕ direction when

- "retrograde" mode: $\text{sgn}(m) = -\text{sgn}(\text{Re}[\omega])$.

Modes with $m = 0$ cannot be labeled as either prograde or retrograde. This is demonstrated in Fig. 1.

When a perturber is corotating with the spin of the black hole, it dominantly excites the prograde modes. For most binary coalescences, the remnant spin ends up with a positive projection onto the direction of the orbital angular momentum at plunge; thus the prograde modes are expected to be most important. In this study, we found that the power of $m \neq 0$ retrograde modes was a very small fraction of the total power, but we nonetheless include them to provide a more complete picture of QNM modeling and attain marginally higher accuracies. Note though that for $m = 0$ modes, neither of the pair of mirror modes is dominant, so both must be included in the fits.

In addition to the frequency, there is also an associated angular mode distribution for a given QNM, which is given by a spin-weighted spheroidal harmonic function $_sS_{\ell m}(\theta, \phi; c)$ that solves the separated angular equation [11]. Here θ and ϕ represent the polar and azimuthal angles, and crucially this is a coordinate system where the black hole is at rest and its spin vector is along the $\theta = 0$ direction.

The complex oblateness parameter $c = a\omega_{\ell mn}$ is determined by both the QNM frequency and the BH's spin parameter $a = |J|/M$, with $0 \leq a < M$ for a horizon to exist. When $c = 0$, a spheroidal harmonic reduces to a spherical harmonic. For a fixed value of c which is purely real or imaginary, we obtain a complete and orthonormal basis of oblate or prolate spheroidal harmonics. However, we have complex values of c, and a different c associated to each QNM, so they may no longer form a complete basis.

Therefore, we choose to work in the complete basis of spin-weighted spherical harmonics. Each spheroidal harmonic can be decomposed as a series of spherical harmonics with the same m but different ℓ as

$$_sS_{\ell' m}(\theta, \phi; c) = \sum_\ell C_{\ell \ell' m}(c) \, _sY_{\ell m}(\theta, \phi), \quad (3)$$

where the $C_{\ell \ell' m}(c)$ functions are called the spherical-spheroidal mixing coefficients [22]. Here we follow the conventions of [15], as implemented in [41]. These conventions are that $\sum_\ell |C_{\ell \ell' m}|^2 = 1$, and that $C_{\ell \ell' m}$ is purely real when $\ell = \ell'$. In the case where $c = 0$, we then have $C_{\ell \ell' m}(0) = \delta_{\ell \ell'}$, i.e., $_sS_{\ell' m}(\theta, \phi; 0) = _sY_{\ell m}(\theta, \phi)$.

With these spheroidal harmonics in mind, we can now write the general ansatz for the strain of a ringing black hole at future null infinity, $h^Q(u, \theta, \phi)$. This ansatz is simply a linear combination of QNMs

$$h^Q(u, \theta, \phi) = \sum_{\ell', m, n, p} \mathcal{A}^p_{\ell' mn} e^{-i\omega^p_{\ell' mn}(u-u_0)}$$
$$_{-2}S_{\ell' m}(\theta, \phi; a\omega^p_{\ell' mn}), \quad (4)$$

where the $\mathcal{A}^p_{\ell' mn}$ are complex amplitudes for each QNM and u_0 is a freely-specified start time of the QNM model. Although these amplitudes transform in a simple way under translations of the retarded time coordinate u and

rotations about the z-axis, they are not rotated by the Wigner-D matrix under more general rotations.

Now we insert the spherical-spheroidal decomposition from Eq. (3) into the spheroidal ansatz of Eq. (4), rewriting it as

$$h^Q(u, \theta, \phi) = \sum_{\ell', m, n, p} \left[\mathcal{A}^p_{\ell' mn} e^{-i\omega^p_{\ell' mn}(u-u_0)} \right.$$
$$\left. \sum_\ell C_{\ell \ell' m}(a\omega^p_{\ell' mn})_{-2}Y_{\ell m}(\theta, \phi) \right]. \quad (5)$$

Since this is now in the spin-weighted spherical harmonic basis, it is ideal for modeling numerical relativity results. Writing the QNM ansatz $h^Q(u, \theta, \phi)$ in spin-weighted spherical harmonics as in Eq. (1) and (using completeness) matching up the coefficients of $_{-2}Y_{\ell m}(\theta, \phi)$, we readily find that the spherical mode-decomposed analytical QNM model is

$$h^Q_{\ell m}(u) = \sum_{\ell', n, p} \mathcal{A}^p_{\ell' mn} e^{-i\omega^p_{\ell' mn}(u-u_0)} C_{\ell \ell' m}(a\omega^p_{\ell' mn}). \quad (6)$$

These $h^Q_{\ell m}$'s do indeed rotate under the Wigner-D matrix since they are expressed in the spin-weighted spherical harmonic basis [45]. Such a rotation is explicitly shown by Eq. (12) of [19] with a couple of subtle differences between that paper and this one. In this work, we use the conventions of [15], where C is the spherical-spheroidal mixing coefficient. Additionally, we do not express ω^- or $C(a\omega^-)$ in terms of their positive frequency counterparts, via

$$C_{\ell \ell' m}\left(a\omega^-_{\ell mn}\right) = C_{\ell \ell' m}\left(-a\left(\omega^+_{\ell, -m, n}\right)^*\right) \quad (7)$$
$$C_{\ell \ell' m}\left(a\omega^-_{\ell mn}\right) = (-1)^{\ell + \ell'} C^*_{\ell, \ell', -m}\left(a\omega^+_{\ell, -m, n}\right). \quad (8)$$

Using this identity, we can restate our Eq. (6) to look like Cook's Eq. (12) [19]. Regardless of the way one writes down this mode-decomposed analytical model, it allows us to consider a ringing black hole with its spin axis oriented in any direction by rotating $h^Q_{\ell m}$.

B. Importance of BMS frames

One important takeaway from the functional form of the QNM model $h^Q_{\ell m}(u)$ in Eq. (6) is the fact that

$$\lim_{u \to +\infty} h^Q_{\ell m}(u) = 0. \quad (9)$$

That is, $h^Q_{\ell m}(u)$ tends to zero at late times, approaching i^+. Consequently, whenever we fit this model to a waveform, our waveform should also decay to zero as the retarded time approaches $+\infty$ in order to obtain reasonable results.

What some readers may not be familiar with is that gravitational waves need not be, and often are not, zero as

$u \to +\infty$, due to an effect which is commonly called *gravitational memory* [46–49]. Fundamentally, gravitational memory can be understood as a persistent physical change to spacetime that is induced by the passage of transient radiation. While there are various types of gravitational memory effects with varying properties (see [50, 51] for more thorough explanations), the one that will strongly impact our ability to model the ringdown of a black hole with QNMs is the *displacement memory* effect. This is because, unlike the other gravitational memories, the displacement memory uniquely corresponds to an overall net change in the strain between the two points i^0 and i^+; that is, the difference $\Delta = h(u \to +\infty) - h(u \to -\infty)$. Consequently, the strain need not return to zero, provided that the memory is nonzero and the strain's value at i^0 does not cancel the memory's value. Fortunately, it turns out that this important problem regarding gravitational memory is only present if one does not account for the frame that a perturbed black hole should be in for proper QNM modeling.

As has been understood since the 1960s, the symmetry group of asymptotic infinity is not the usual Poincaré group, but a group with a richer structure called the Bondi-van der Burg-Metzner-Sachs (BMS) group [34, 35]. The BMS group is a semidirect product of the usual Lorentz group with an infinite-dimensional group of transformations called supertranslations, which are angle-dependent time advances/delays that contain the familiar spacetime translations as a subgroup. Fundamentally, supertranslations act on the Bondi coordinates (u, r, θ, ϕ) as

$$u' = u - \alpha(\theta, \phi). \tag{10}$$

and the strain as

$$\begin{aligned} h'(u', \theta, \phi) &= h(u', \theta, \phi) - \bar{\eth}^2 \alpha(\theta, \phi) \\ &= \sum_{k=0}^{\infty} \frac{1}{k!} \left(-\alpha(\theta, \phi) \frac{\partial}{\partial u} \right)^k h(u, \theta, \phi) - \bar{\eth}^2 \alpha(\theta, \phi). \end{aligned} \tag{11}$$

where $\bar{\eth}$ is the conjugate of the Geroch-Held-Penrose differential spin-weight operator [52]. Above

$$\alpha(\theta, \phi) \equiv \sum_{\ell \geq 0, |m| \leq \ell} \alpha_{\ell m} Y_{\ell m}(\theta, \phi) \tag{12}$$

with

$$\alpha_{\ell m} = (-1)^m \bar{\alpha}_{\ell, -m} \tag{13}$$

is a real function which characterizes the supertranslation. The $\ell = 0$ component of $\alpha(\theta, \phi)$ is a time translation, the $\ell = 1$ components are space translations, and the $\ell \geq 2$ are proper supertranslations. From Eq. (11), one can easily realize that under the action of a supertranslation the strain experiences two types of changes. First, the strain is changed by the angle-dependent constant $\bar{\eth}^2 \alpha(\theta, \phi)$. Apart from this, however, because the retarded time

changes as $u' = u - \alpha(\theta, \phi)$, we also expand about u to express the transformed strain directly in terms of the strain in the original frame. We see from Eq. (11) that this involves multiplying the time derivatives of the strain with powers of $\alpha(\theta, \phi)$. Consequently, the strain will experience mode-mixing in addition to changing by an angle-dependent constant. Furthermore, if one imagines taking a time-derivative of Eq. (11) then it can be seen that the news will also experience mode-mixing due to the supertranslation's effect on the retarded time.

Therefore, because of these extra symmetries, whenever we examine a system that is radiating gravitational waves it is insufficient to specify just a Poincaré frame, e.g., the remnant BH's center-of-mass frame; we instead need to specify the entire BMS frame, i.e., how the system's supertranslation freedom is being fixed in addition to the usual Poincaré transformations.

In [33] this task of specifying a system's BMS frame was performed for the first time by mapping numerical waveforms from BBH systems to the post-Newtonian (PN) BMS frame, i.e., the frame that PN waveforms are in. When fitting the ringdown phase of waveforms to Eq. (6), mapping waveforms to the PN BMS frame is not the appropriate BMS frame choice, because this frame corresponds to the strain going to zero at early times (when approaching i^0), rather than at late times (when approaching i^+). Instead, we should be mapping our waveforms to what is called the *nice section* [39] or the *super rest frame* [33] at i^+. This is because when Teukolsky found the linear equations that describe the dynamical gravitational perturbations of a rotating black hole [11], i.e., the equations that give rise to QNMs, he implicitly worked in the BMS frame adapted to the stationary background metric [53], i.e., the super rest frame. However, black holes in nature or the remnant black holes produced in numerical simulations are supertranslated relative to this preferred frame. As a result, we need to map these black holes to the frame that Teukolsky worked in.

As outlined in [33], the way to map a system to the super rest frame is to use the Moreschi supermomentum, which is an extension of the usual Bondi four-momentum,

$$\Psi^{\mathrm{M}}(u, \theta, \phi) = \sum_{\ell \geq 0, |m| \leq \ell} \Psi_{\ell m}^{\mathrm{M}}(u) Y_{\ell m}(\theta, \phi), \tag{14}$$

where

$$\Psi_{\ell m}^{\mathrm{M}}(u) = -\frac{1}{\sqrt{4\pi}} \int_{S^2} Y_{\ell m} \left[\Psi_2 + \sigma \dot{\bar{\sigma}} + \eth^2 \bar{\sigma} \right] d\Omega, \tag{15}$$

Ψ_2 is one of the Weyl scalars, and σ is the shear.[5] Ideally, to map to the super rest frame we would want to minimize the Moreschi supermomentum as $u \to +\infty$. But, since our

---

[5] Note that here and in Eq. (15) we are specifically working with the Moreschi-Boyle convention [33, 36, 54, 55], i.e., in comparison to the numerical formulation of the strain and the Weyl scalars we simply have $h^{\mathrm{NR}} = 2\bar{\sigma}$ and $\Psi_i^{\mathrm{NR}} = \frac{1}{2}(-\sqrt{2})^i \Psi_i$.

simulations do not go all the way to i^+, we can instead minimize the Moreschi supermomentum during a late portion of the ringdown phase. Specifically, we construct the BMS frame of our waveforms via the following:

- take the boost velocity and space translation, i.e., the $\ell = 1$ components of the supertranslation, to be the transformations that minimize the remnant's center-of-mass charge over the late time window $u \in [u_{\mathrm{peak}} + 150M, u_{\mathrm{peak}} + 350M]$ [33];

- take the $2 \leq \ell \leq 4$ modes of the supertranslation to be the transformations that minimize the L^2 norm of the $2 \leq \ell \leq 4$ modes of Ψ^{M} over the late time window $u \in [u_{\mathrm{peak}} + 150M, u_{\mathrm{peak}} + 350M]$ [33];

- fix the system's rotation freedom by aligning the remnant BH's spin with the positive z-axis.

These calculations for fixing the BMS frame require the system's strain as well as the four Weyl scalars Ψ_{1-4} [33]. Note that while only the strain, Ψ_1, and Ψ_2 are needed to compute the BMS charges, Ψ_3 and Ψ_4 are also needed to transform Ψ_1 and Ψ_2 during the frame fixing procedure. We obtain the Ψ_3 and Ψ_4 Weyl scalars independently from the strain through our Cauchy-characteristic extraction. Above u_{peak} is the time at which the L^2 norm of the strain achieves its maximum value. By performing this frame-fixing procedure, we transform to a waveform with its BMS frame fixed so that it can be modeled by Eq. (6). Note that the window $u \in [u_{\mathrm{peak}} + 150M, u_{\mathrm{peak}} + 350M]$ is chosen as such because it is roughly the $200M$ before the earliest end time of our simulations. We find that our results are fairly independent of this time window, provided that it starts beyond $u \approx (u_{\mathrm{peak}} + 100M)$. A quantitative description of how the results are affected by the choice of time window is beyond the scope of this paper. Nevertheless, an analysis of when to map to the super rest frame will be presented in future work.

C. QNM fitting procedure

Given a numerical waveform $h_{\ell m}^{\mathrm{NR}}(u)$ and the functional form of $h_{\ell m}^Q(u)$, we can consider the problem of fitting for the complex QNM amplitudes $\mathcal{A}_{\ell' m n}^p$. To do this, we first need an inner product on the space of spin-weight s waveforms on $\mathscr{I}^+$. For waveforms a and b, the natural inner product is defined as

$$\langle a, b \rangle \equiv \int_{u_0}^{u_f} du \int_{S^2} d\Omega \, a^*(u, \theta, \phi) b(u, \theta, \phi), \quad (16)$$

Where $[u_0, u_f]$ is the interval of time where we would like to fit the waveform with a QNM model. Both waveforms can be decomposed into $a_{\ell m}$ and $b_{\ell' m'}$ as in Eq. (1). By applying the orthogonality relationship of Eq. (2) to collapse the double sum to a single sum, the inner product

on $\mathscr{I}^+$ then becomes

$$\langle a, b \rangle = \int_{u_0}^{u_f} du \sum_{\ell, m} a_{\ell m}^*(u) b_{\ell m}(u) = \sum_{\ell, m} \langle a_{lm}, b_{lm} \rangle_u,$$
$$(17)$$

where

$$\langle f, g \rangle_u \equiv \int_{u_0}^{u_f} f^*(u) g(u) du \quad (18)$$

is the usual L^2 inner product for complex functions on the real line. However, because our study only considers modes with $\ell \leq 4$, the inner product that we use in the rest of paper is in fact given by

$$\langle a, b \rangle = \sum_{\ell \leq 4, m} \langle a_{lm}, b_{lm} \rangle_u, \quad (19)$$

which we henceforth call the all-mode inner product, keeping in mind that here 'all' means all the modes included in the NR waveform.

From this inner product we construct the mismatch $\mathcal{M}$, a figure of merit commonly used in the literature, as follows:

$$\mathcal{M}(a, b) \equiv 1 - \mathcal{O}(a, b), \quad (20)$$

where $\mathcal{O}(a, b)$ is the overlap,

$$\mathcal{O}(a, b) \equiv \mathrm{Re}\left[\frac{\langle a, b \rangle}{\sqrt{\langle a, a \rangle \langle b, b \rangle}} \right]. \quad (21)$$

Consequently, for a NR waveform $h^{\mathrm{NR}}(u, \theta, \phi)$ expressed by its spin-weighted spherical harmonic coefficients $h_{\ell m}^{\mathrm{NR}}$, we can quantify the effectiveness of a fit $h^Q(\vec{\lambda})$ by calculating the all-mode mismatches $\mathcal{M}(h^{\mathrm{NR}}, h^Q(\vec{\lambda}))$. Here $\vec{\lambda}$ is the set of free parameters of the fit. When we focus on a single mode (ℓ, m), however, we instead use the single mode mismatch $\mathcal{M}(h_{\ell m}^{\mathrm{NR}}, h_{\ell m}^Q(\vec{\lambda}))$.

Nonetheless, we do not find the optimal parameters $\vec{\lambda}_{\mathrm{opt}}$ by directly minimizing this figure of merit. Instead we first calculate the residual

$$R \equiv h^{\mathrm{NR}} - h^Q, \quad (22)$$

and then compute the squared norm of the residual, $\langle R, R \rangle$, as the figure of merit that we want to minimize. One can show that because the norm of $h^Q(\vec{\lambda})$ can be independently varied, minimizing the norm of the residual also minimizes the mismatch. However the problem of minimizing the former is manifestly linear in nature for the QNM amplitudes, and is not degenerate in the norm. Therefore we find the optimal parameters $\vec{\lambda}_{\mathrm{opt}}$ by

$$\vec{\lambda}_{\mathrm{opt}} = \arg\min_{\vec{\lambda}} \langle R, R \rangle \quad \text{or} \quad \vec{\lambda}_{\mathrm{opt}} = \arg\min_{\vec{\lambda}} \langle \dot{R}, \dot{R} \rangle, \quad (23)$$

where we use the second choice if we want to work in the domain of the news $\mathcal{N} = \dot{h}$. Although one could also

consider working in the Ψ_4 domain, our analyses focus on the strain, since it is the physical quantity that the gravitational-wave detectors measure and on the news, since the power is naturally defined by it.

Now, $\vec{\lambda}$ can take on one of two forms: $\vec{\lambda} = \{\mathcal{A}^p_{\ell'mn}\}$, or $\vec{\lambda} = \{\{\mathcal{A}^p_{\ell'mn}\}, M, a\}$, where $\mathcal{A}^p_{\ell'mn}$ are the QNM amplitudes from Eq. (6), and M and a are the mass and spin of the remnant black hole. In the former we use the remnant black hole's mass and spin obtained from the simulation (see below), and solve for $\vec{\lambda} = \{\mathcal{A}^p_{\ell'mn}\}$ using NumPy's linear least square method [56]. On the other hand when $\vec{\lambda} = \{\{\mathcal{A}^p_{\ell'mn}\}, M, a\}$, the remnant properties are deduced by fitting the waveform. Here we perform a least-squares minimization between the NR waveform and the QNM model using SciPy's Nelder-Mead algorithm [57, 58] to find the remnant BH's mass and spin and simultaneously use the linear least square method to determine the amplitudes. We also note that since we rotate the remnant BH's spin direction to be aligned with the positive z-axis, there is no mixing of the m modes. Therefore, we can fit the QNM amplitudes for each value of m independently.

Finally, it should be noted that when we are only solving for the amplitudes, i.e., $\vec{\lambda} = \{\mathcal{A}^p_{\ell'mn}\}$, we obtain the mass and the spin of the remnant from $\mathscr{I}^+$ rather than the apparent horizon. That is, following the work of [33, 59], we use Poincaré charges to obtain the remnant's mass and spin via Eqs. (11) and (15) of [59]. The mass and spin are taken to be the values of the charges at the last available time step.

D. Numerical waveforms

For the following results, we numerically evolved a set of 14 binary black hole mergers with many mass ratios and spin configurations using the Spectral Einstein Code (SpEC) [62]. We list the important parameters of these various BBH systems in Table I. Each simulation contains roughly 19 orbits prior to merger and is evolved until the waves from ringdown leave the computational domain. Unlike the evolutions in the SXS catalog, the full set of Weyl scalars and the strain have been extracted from these runs and the waveforms have been computed using the extrapolation technique described in [63] and the Cauchy-characteristic extraction (CCE) procedure that is outlined in [64, 65]. Extrapolation is performed with the python module scri [36, 66–68] and CCE is run with SpECTRE's CCE module [64, 65, 69].

For the CCE extractions, the four world tubes that are available have radii that are equally spaced between $2\lambda_0$ and $21\lambda_0$, where $\lambda_0 \equiv 1/\omega_0$ is the initial reduced gravitational wavelength as determined by the orbital frequency of the binary from the initial data. Based on the recent work of [70], however, we choose to use only the waveforms that correspond to the world tube with the second-smallest radius, since these waveforms have been shown to minimally violate the BMS balance laws.

For clarity, we provide the world tube radius used for each system in Table I. All of these 14 BBH systems' waveforms have been made publicly available at [60, 61].

As mentioned above, the asymptotic strain waveforms are computed using two methods: extrapolation and CCE. The first method utilizes Regge-Wheeler-Zerilli (RWZ) extraction to compute the strain on a series of concentric spheres of constant coordinate radius and then proceeds to extrapolate these values to future null infinity $\mathscr{I}^+$ using $1/r$ approximations [7, 63, 71–74]. This is the strain that can be found in the public SXS catalog. The other and more faithful extraction method, which is known as CCE, computes the strain by using the world tube data provided by a Cauchy evolution as the inner boundary data for a nonlinear evolution of the Einstein field equations on null hypersurfaces extending all the way to $\mathscr{I}^+$ [64, 65]. CCE requires freely specifying the strain on the initial null hypersurface labeled $u = 0$. Like [33, 50, 70], we choose this field to match the value and the first radial derivative of h from the Cauchy data on the world tube using the ansatz

$$h(u = 0, r, \theta^A) = \frac{A(\theta^A)}{r} + \frac{B(\theta^A)}{r^3}, \qquad (24)$$

where the two coefficients $A(\theta^A)$ and $B(\theta^A)$ are fixed by the Cauchy data on the world tube.

Lastly, when performing our analyses, we predominantly use the code scri [36, 66–68] to compute Poincaré charges and transform our asymptotic waveform quantities to the super rest frame using the procedures outlined in Sec. II and Appendix A of [33]. Our waveforms only include the $\ell \leq 4$ modes since these are the modes included in the BMS frame fixing procedure. We also only model our waveforms up to $u_f = u_{\text{peak}} + 90\,M$ as in [18].

III. ON WHICH MODES TO INCLUDE

The importance of using multiple waveform modes to capture the physics of a remnant black hole—considering both multiple angular (ℓ, m) modes as well multiple overtones—has been studied extensively [18–20, 26, 75]. When constructing a QNM model it is crucial that we are able to choose as many modes as necessary to accurately model our system, without overfitting or introducing degeneracy. Because manually choosing an arbitrary number of modes without knowing which modes are important to include is objectionable, we have written a greedy algorithm that provides us with an efficiently low number of modes needed to model the ringdown waveform to a requested precision. Consequently, we can reduce the number of modes that are needed to capture the most physics and also identify the most physically-relevant modes.

Name	CCE radius	q	χ_A:	$(\hat{x},$	$\hat{y},$	$\hat{z})$	χ_B:	$(\hat{x},$	$\hat{y},$	$\hat{z})$
q1_nospin	292	1.0		(0,	0,	0)		(0,	0,	0)
q1_aligned_chi0_2	261	1.0		(0,	0,	0.2)		(0,	0,	0.2)
q1_aligned_chi0_4	250	1.0		(0,	0,	0.4)		(0,	0,	0.4)
q1_aligned_chi0_6	236	1.0		(0,	0,	0.6)		(0,	0,	0.6)
q1_antialigned_chi0_2	274	1.0		(0,	0,	0.2)		(0,	0,	-0.2)
q1_antialigned_chi0_4	273	1.0		(0,	0,	0.4)		(0,	0,	-0.4)
q1_antialigned_chi0_6	270	1.0		(0,	0,	0.6)		(0,	0,	-0.6)
q1_precessing	305	1.0		(0.487,	0.125,	-0.327)		(-0.190,	0.051,	-0.227)
q1_superkick	270	1.0		(0.6,	0,	0)		(-0.6,	0,	0)
q4_nospin	235	4.0		(0,	0,	0)		(0,	0,	0)
q4_aligned_chi0_4	222	4.0		(0,	0,	0.4)		(0,	0,	0.4)
q4_antialigned_chi0_4	223	4.0		(0,	0,	0.4)		(0,	0,	-0.4)
q4_precessing	237	4.0		(0.487,	0.125,	-0.327)		(-0.190,	0.051,	-0.227)
SXS:BBH:0305 (GW150914)	267	1.221		(0,	0,	0.330)		(0,	0,	-0.440)

TABLE I. Parameters of the BBH mergers used in our results. The mass ratio is $q = M_A/M_B$, and the initial dimensionless spins of the two black holes are χ_A and χ_B. These simulations have been made publicly available at [60, 61].
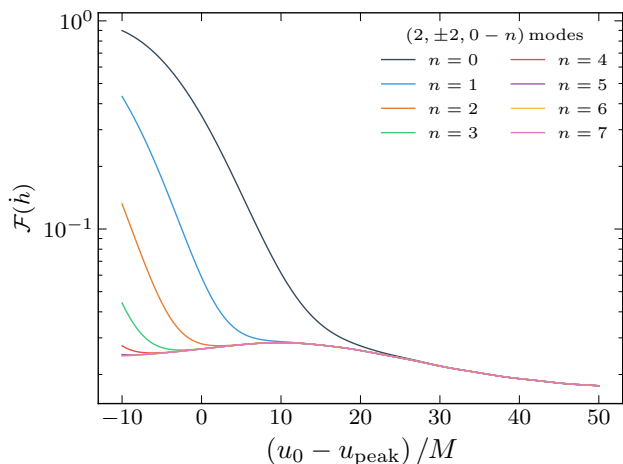

FIG. 2. Fraction of unmodeled power that is obtained when comparing a QNM model built from the $(2, \pm 2, 0 - n)$ mode(s) to a CCE strain waveform as a function of the QNM model start time u_0. We compute the fraction of unmodeled power in the waveform using the news waveforms, i.e., by using Eq. (30). This includes the power that is unmodeled because of neglecting higher modes in the QNM model. BBH merger: SXS:BBH:0305.
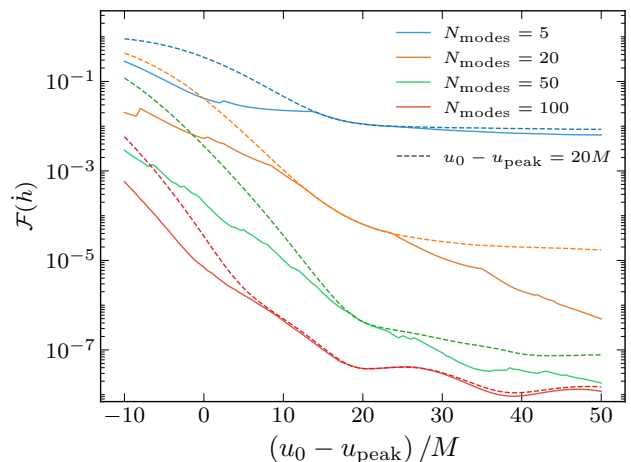

FIG. 3. Fraction of unmodeled power (solid) that is obtained when comparing QNM models built by our greedy algorithm with various number of modes to a CCE strain waveform. Again, the power, which is plotted and used in our algorithm to pick modes to model, is computed using the news waveforms, i.e., by using Eq. (30). The dashed curves are QNM fits using the fixed set of modes determined by the greedy algorithm at the time $u_0 - u_{\text{peak}} = 20M$. On the other hand, the solid curves have their set of modes determined for each u_0 independently, which causes these curves to not be smooth. BBH merger: SXS:BBH:0305.

A. Greedy algorithm

The greedy algorithm that we implement is iterative, adding the prograde and retrograde modes at each iteration. The data at iteration i is a collection of i mode labels (ℓ', m, n, p) and the parameter vector of length i,

$$\vec{\lambda}^{(i)} = \{\mathcal{A}^p_{\ell'mn}\}, \qquad (25)$$

corresponding to those modes.

The greedy algorithm can be summarized as follows.

(I) Begin with an empty list of modes and amplitudes.

(II) At each iteration i, form the residual

$$R^{(i)} \equiv h^{\text{NR}} - h^{Q,i}, \qquad (26)$$

between the NR waveform and $h^{Q,i}$, which is built from the i amplitudes $\{\mathcal{A}^p_{\ell'mn}\}$. If instead working

in the news domain, we form the residual as the difference of the news waveforms

$$\dot{R}^{(i)} \equiv \dot{h}^{\mathrm{NR}} - \dot{h}^{Q,i} \, . \tag{27}$$

(III) Compute the power in each mode of the residual,

$$P_{\ell m}^{(i)}(R) \equiv \langle R_{\ell m}^{(i)}, R_{\ell m}^{(i)} \rangle_u \, , \tag{28}$$

using the usual L^2 metric in Eq. (18). Analogously, when working in the news domain we use $P_{\ell m}^{(i)}(\dot{R})$ as the power instead. Notice that, $\sum_{\ell,m} P_{\ell m}^{(i)}(\dot{R})$ is proportional to the physical gravitational-wave luminosity of the residual waveform.

(IV) Rank the (ℓ, m) modes in the residuals by their powers $P_{\ell m}^{(i)}$, and identify the mode $(\bar{\ell}, \bar{m})$ with the largest residual power.

  (1) If no QNMs with the $(\ell = \bar{\ell}, m = \bar{m})$ mode are present in the parameter list, add the prograde and retrograde modes $(\bar{\ell}, \bar{m}, 0, \pm 1)$.

  (2) If some QNMs with $(\ell = \bar{\ell}, m = \bar{m})$ are already in the parameter list, identify the smallest $\bar{n}$ not present in the parameter list. If $\bar{n} \leq n_{\max}$ for some max overtone number $n_{\max}$, add this next mode with the prograde and retrograde modes $(\bar{\ell}, \bar{m}, \bar{n}, \pm 1)$. For this paper we chose a max overtone number of $n_{\max} = 7$.

  (3) If all modes $(\bar{\ell}, \bar{m})$ with $0 \leq n \leq n_{\max}$ are already in the parameter list, set $(\bar{\ell}, \bar{m})$ as the mode of the residual that is the next loudest in the list of $P_{\ell m}^{(i)}$. Return to step (1) to find which mode to include.

Although here at each step we are adding 2 QNMs $(\bar{\ell}, \bar{m}, \bar{n}, \pm 1)$, we group these modes together and count them as adding one mode.

 (V) After identifying the next mode(s) to include, re-solve the linear least squares problem to determine the optimal values of $\{\mathcal{A}_{\ell' mn}^p\}$.

(VI) Compute the fraction of residual power to target waveform power in the strain domain

$$\mathcal{F}(h) \equiv \frac{\langle R^{(i)}, R^{(i)} \rangle}{\langle h^{\mathrm{NR}}, h^{\mathrm{NR}} \rangle} \tag{29}$$

or the news domain

$$\mathcal{F}(\dot{h}) \equiv \frac{\langle \dot{R}^{(i)}, \dot{R}^{(i)} \rangle}{\langle \dot{h}^{\mathrm{NR}}, \dot{h}^{\mathrm{NR}} \rangle} \, , \tag{30}$$

where R and $\dot{R}$ are defined in Eq. (26) and Eq. (27). Both of these choices are well motivated, but we primarily use Eq. (30), since this corresponds to the physical gravitational-wave luminosity of the residual waveform.

(VII) Terminate if either $\mathcal{F} < \mathcal{F}_{\mathrm{target}}$ for some target residual power fraction, or if the number of modes $i = N_{\max}$: a maximum number of modes to include.

(VIII) Return to step (II) and repeat.

A study using multimode fitting to investigate the performance of three different fitting methods across three different sets of modes—$\{(2,2)\}, \{(2,2), (3,2)\}, \{(2,2), (3,2), (4,2)\}$—was recently carried out in [19]. Results show that when fitting for more than just the dominant $(2,2)$ mode, all fitting methods converge. However, these methods are tested using only a limited set of modes, whereas our greedy algorithm can use all modes (see [19] for more details).

Earlier studies of multimode fitting have been carried out in one of two ways: some models have been executed by manually choosing a set of modes [18, 19, 24] while others use greedy algorithms to pick which modes to model [20, 26]. However, instead of focusing on a single (ℓ, m) mode as in [20] or greedily picking only the angular numbers (ℓ, m) as in [26], we implement a physically well motivated, multimode greedy algorithm where each QNM with labels (ℓ, m, n) is picked greedily. At the moment, checks to compare greedy algorithms with one another have not been performed. This would be interesting to examine in the future.

B. Importance of multiple modes in modeling

In the remaining parts of this section, we use the simulation SXS:BBH:0305, which corresponds to GW150914, (see Table I) to study the importance of multimode fitting. We begin by applying our QNM modeling procedure to the $(2, \pm 2)$ modes with up to 7 overtones. In Fig. 2 we show the fraction of unmodeled power as a function of $u_0 - u_{\mathrm{peak}}$ using n number of overtones in the QNM model. For computing the unmodeled power, we use the CCE waveform, in the super rest frame, and measure the fraction of unmodeled power in the news domain with Eq. (30). From this plot, one can easily observe the importance of including overtones in the model. By using just the $n = 0$ mode, one can only model about 65% of the power starting at $u_0 = u_{\mathrm{peak}}$. With all 7 of the overtones included, the modeled power improves to roughly 97% of the total power. Note, however, that these numbers will vary depending on the time that one chooses to model the QNMs.

Accounting for overtones, however, is only one of the important components for correctly modeling a waveform with QNMs. Although the $(2, \pm 2)$ modes are the most important to use due to their dominance, including higher-order modes is crucial to more accurately describe the ringdown phase. This is especially true for systems that may not exhibit symmetries, e.g., having mass ratio one. Overall, higher-order modes contain less power and overtones have shorter damping times relative to the $(2, \pm 2)$ modes and $n = 0$ modes. Therefore, their
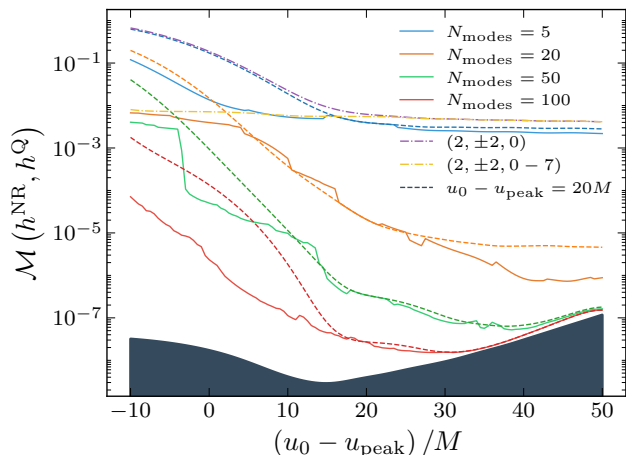
FIG. 4. All-mode mismatches between the CCE waveform and a QNM model fitting N number of modes. The solid curves correspond to QNM models with a varying number of modes that are modeled. The dashed curves are QNM amplitude fits using the modes from $u_0 - u_{\text{peak}} = 20M$. The dash-dotted curves represent the all-mode mismatches from just the $(2, \pm2)$ modes—one with the $n = 0$ tone and another with the $n = 0 - 7$ tones. Finally, the top of the black region illustrates the mismatch between the highest and the next-highest resolution waveforms to provide a reference for the numerical error that is present in our strain waveform. BBH merger: SXS:BBH:0305.

importance within the QNM model lessens as we reach later stages of ringdown. Nevertheless, they exhibit a considerable amount of power at early ringdown times and are essential in capturing the remaining power stored in a gravitational wave. To highlight this, in Fig. 3 we compute the fraction of unmodeled power for models that include $N \in \{5, 20, 50, 100\}$ modes as a function of the QNM model's start time u_0. We remind the reader that N counts the number of pairs of prograde and retrograde (ℓ, m, n) modes included by the greedy algorithm, e.g., the set $\{(2, 2, 0, \pm1), (2, 2, 1, \pm1), (3, 2, 0, \pm1)\}$ corresponds to $N = 3$. In this plot, the solid curves correspond to running the greedy algorithm independently for each u_0, while the dashed curves just use the fixed set of modes that are obtained by the greedy algorithm at $u_0 - u_{\text{peak}} = 20M$. The jaggedness of the solid curves illustrates the fact that the greedy algorithm's choice of modes for the QNM model is not a smooth function of the model start time u_0. Moreover, we have performed a minimal test of the greedy algorithm to ensure that the results do not depend too sensitively on the initial mode content. We do this by giving the greedy algorithm an initial set of modes to fit before it adds the modes it has ranked. Slight changes in results only arise when modeling a small number of modes, e.g., $N = 5$ at times before $u_0 = u_{\text{peak}}$. This is not surprising since overtones play an important role at early times. Consequently, replacing an overtone with a higher harmonic at such times would slightly worsen our

model by increasing the fraction of unmodeled power. For a higher number of modes N and later times, however, no detectable change occurs.

Using the solid curves, we find that at $u_0 = u_{\text{peak}}$ the power captured in the model is nearly 96% with 5 modes, which is a rather comparable result to using the $(2, \pm2, 0 - 7)$ modes. With 20 modes over 99% of the power is captured. With 100 modes, we are modeling 99.999% of the power. Again, for this plot we are using the CCE waveform for SXS:BBH:0305 and are performing computations of the power in the news domain by using Eq. (30). The order in which all 168 modes of this waveform are included is shown in Table. II.

Apart from the fraction of unmodeled power, we also calculate the mismatches between the CCE strain and the model using varying number of modes, as shown by the solid curves in Fig. 4. As a reference, we also provide two dash-dotted curves showing the all-mode mismatches from just the $(2, \pm2)$ modes—one with the $n = 0$ tone and another with the $n = 0 - 7$ tones. Moreover, we show the mismatch between the highest and the next-highest resolution waveforms via the top of the black region to illustrate that every mismatch curve is above our numerical error, and thus, there is no concern for overfitting to numerical noise.

Our most important finding regarding multimode fitting, however, is that by using multimode fitting rather than just the $(2, 2)$ mode with its $n = 0$ tone and the first 7 overtone modes we can significantly improve our ability to extract the remnant's mass and spin using a QNM model. To confirm that our QNM model is able to faithfully represent the full numerical simulation, rather than just the waveform, we perform a minimization of the residual between the QNM model and the NR strain waveform, with the remnant's mass and spin as free parameters. As a measure of the error in the mass and spin found by our NR/QNM mismatch minimization procedure, we use

$$\epsilon = \sqrt{(\delta M/M)^2 + (\delta\chi)^2}, \tag{31}$$

where the terms δM and $\delta\chi$ are the differences between the minimization results and the remnant values obtained by computing the Poincaré charges that correspond to the strain and Weyl scalars produced by the simulation (see Sec. II C and Eqs. (11) and (15) of [59]). Our results from this procedure are shown in Fig. 5.

For this analysis, we used 86 SXS simulations that were incorporated into the NRHyb3dq8 surrogate [76]. In this figure, there are four histograms that show the epsilon values obtained from either using the $(2, 2, 0)$ mode, the $(2, 2, 0 - 3)$ modes, the $(2, 2, 0 - 7)$ modes, or from using the first 40 modes that are chosen by our multimode algorithm, which is summarized in Sec. III A. For each of these histograms, we also plot the median of the epsilons on the ϵ-axis. However, as can be seen by using just 40 modes, we can improve the median epsilon estimate across these simulations by a more than half an order of magnitude: specifically, the median epsilon that is obtained from the $(2, 2)$ mode with up to 7 overtones

11

ℓ	2								3								4							
n / m	0	1	2	3	4	5	6	7	0	1	2	3	4	5	6	7	0	1	2	3	4	5	6	7
-4																	12	14	18	31	38	50	69	90
-3									10	16	33	43	83	112	153	168	44	48	56	71	99	116	130	152
-2	2	4	6	25	55	104	135	156	26	28	34	47	80	114	148	164	75	77	84	97	107	118	143	160
-1	19	22	39	62	101	127	145	161	63	66	73	94	109	121	132	139	123	125	133	137	141	149	158	166
0	7	8	21	36	41	59	79	95	52	53	58	60	65	78	91	103	86	87	88	92	100	106	111	120
1	20	23	40	61	102	128	146	162	64	67	72	93	110	122	131	140	124	126	134	138	142	150	157	165
2	1	3	5	24	54	105	136	155	27	29	35	46	81	115	147	163	74	76	85	96	108	119	144	159
3									9	15	32	42	82	113	154	167	45	49	57	70	98	117	129	151
4																	11	13	17	30	37	51	68	89

TABLE II. Order in which 168 (ℓ, m, n) modes are added to the QNM model by the greedy algorithm for `SXS:BBH:0305` with the QNM model's start time u_0 taken to be $u_{\rm peak}$, i.e., the peak of the L^2 norm of the strain.
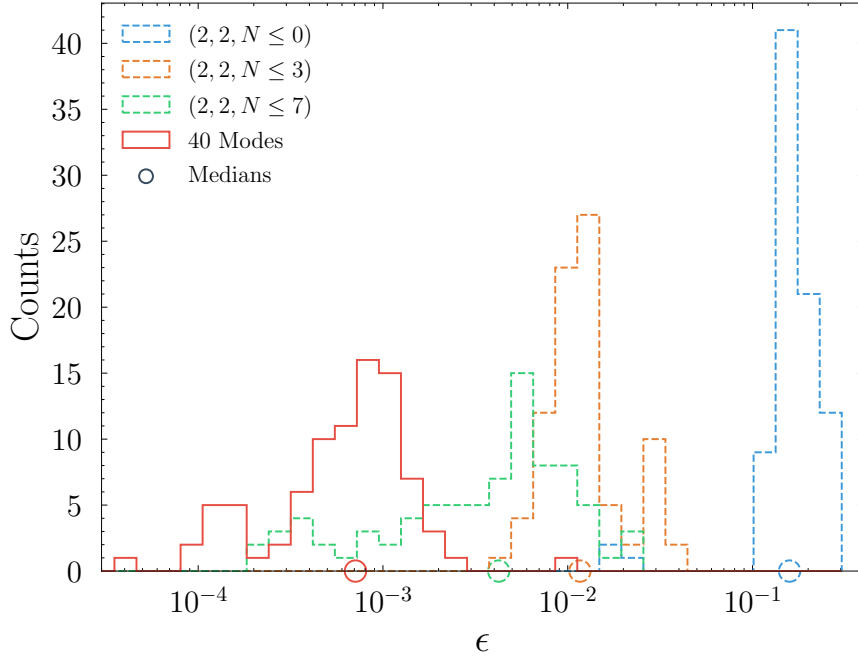

FIG. 5. Various distributions of the epsilons (see Eq. (31)) that have been obtained by minimizing the residual between the strain waveforms from 86 SXS simulations used in the `NRHyb3dq8` surrogate and a QNM model that has either been built with the $(2,2,0)$ mode (blue), the $(2,2,0-3)$ modes (orange), the $(2,2,0-7)$ modes, (green), or the 40 modes that are chosen by the multimode algorithm (red) (see Sec. III A). On the ϵ-axis, we also provide the median values of epsilon for each distribution. The starting time for the distributions created using the $(2,2)$ mode and various overtones is taken to be $u_0 - u_{\rm peak} = 0M$ while for the distribution created using 40 modes as chosen by the greedy algorithm it is $u_0 - u_{\rm peak} = 20M$.

is 4.23×10^{-3} while the median epsilon obtained from using 40 modes is 7.10×10^{-4}. Furthermore, we find that the median epsilon only improves as one includes more than 40 modes, but eventually reaches a minimum value of 2.68×10^{-4} when using every mode available in the waveform. We attribute this inability to push the epsilon precision any lower to the fact that the higher-order modes of the waveform are more influenced by numerical error and also have more nonlinear contributions, which are not captured by the linear QNM model (see, e.g., Fig. 2 of [50]). Finally, we should also note that when using modes other than just the $(2,2)$ mode, the QNM model needs to start at a time later than the usual $u_0 - u_{\rm peak} = 0$. This is because other modes, such as $m = 0$ modes, exhibit nonlinearities related to memory effects that cannot be represented by the QNM model. Consequently, for the histogram created with 40 modes that we show in Fig. 5, we start our fits at $u_0 - u_{\rm peak} = 20M$.

IV. CONSEQUENCES OF WORKING IN THE SUPER REST FRAME

At this point, we now wish to illustrate the importance of using waveforms that are in the super rest frame and clarify some points of disagreement that have been present in recent works regarding QNMs. As a reminder, in this work by super rest frame we mean the frame in which the boost velocity and space translation are fixed by minimizing the center-of-mass charge, the $2 \leq \ell \leq 4$ supertranslations are fixed by minimizing the L^2 norm of the $2 \leq \ell \leq 4$ modes of the Moreschi supermomentum (see Sec. II B), and the rotation is fixed by aligning the remnant BH's spin with the positive z-axis. First, we simply show the most prominent effect that working in the incorrect BMS frame has on QNMs. In Fig. 6, we show two plots. Both are comparisons between the real component of the strain $(2, 0)$ mode of the CCE waveform that corresponds to the GW150914 event and a QNM model for the same mode with 7 overtones. However, the plots on the left use the waveform in the remnant BH's center-of-mass frame whereas the plots on the right use the waveform once it has been mapped to the super rest frame. As can be seen, the primary difference between these two curves is that the curve on the left approaches some nonzero value as $u \to +\infty$ while the curve on the right instead approaches zero. Consequently, the QNM model in the left plot completely fails, while the QNM model in the right plot is what we would expect to see based on QNM fits to the $(2, 2)$ mode, e.g., Fig. 2 of [18]. Again, the reason for this stark contrast in results is due to the supertranslation freedom that is present in our asymptotic waveforms. If one does not map their system to the super rest frame, i.e., if one does not make their system resemble a Kerr black hole in its canonical BMS frame—rather than a supertranslated Kerr black hole— then the QNM model fails to represent the waveform.

Apart from this, in the bottom right plot of Fig. 6 we also provide the red curve to highlight the importance of performing supertranslations, i.e., transforming the coordinates as well as the waveform objects, rather than just changing the strain by a constant. This curve also shows the residual between a NR waveform and its corresponding best-fit QNM model, but the NR waveform has been changed by a constant so that its final value is zero, as was performed in Giesler et al. [18]. As can be seen, while the error in this QNM fit is comparable to that of the NR waveform whose BMS frame has been properly fixed, it is still off by nearly an order of magnitude. Therefore, even though changing the strain by a constant is simpler than performing a BMS transformation, applying a supertranslation produces a much better QNM fit because it also fixes unwanted mode-mixing that occurs due to the supertranslation also changing the retarded time [36].

While this effect is most prominent in the strain $(2, 0)$ mode, it is also present in other modes, such as the $(3, 2)$ as shown by Fig. 7, and even the more-commonly used strain $(2, 2)$ mode, as shown by Fig. 8. Note that in Fig. 8

we also provide the purple curve in the bottom right plot, which shows the previous result obtained by [23, 25] when using an extrapolated waveform that has been changed by a constant so that its final value is zero. By comparing the black and purple curves in Fig. 8, one can see that previous studies that have used the $(2, 2)$ mode from the extrapolated waveforms are only slightly impacted by mapping to the super rest frame. However, we will see later that for higher modes this is not true.

In Fig. 9, we show the mismatch in the $(2, 2)$ mode between a numerical waveform and a QNM model, with varying numbers of overtones, as a function of the QNM model's start time u_0. Ultimately, this plot is a recreation of Fig. 1 in [18] or Fig. 2 in [19], but with the intent of clarifying why the figures from those two papers are in clear contrast with one another, despite using the same SXS waveform. In [18], their plot more closely resembles our solid curves, which have been created using a CCE waveform that has been mapped to the super rest frame. In [19], their plot is identical to our dashed curves, which have been created using the publicly available extrapolated waveform that can be found in the SXS Catalog [7, 61]. This is the waveform used in [18, 19], without one important change. What is different about the data used in [18] is that they performed an ad hoc subtraction of their waveform to send it to 0 as $u \to +\infty$. In [19] and in the dashed curves of Fig. 9, this subtraction was not performed, hence the worsening of the mismatch that can be seen as u_0 increases. The reason why our solid curves more closely resemble the curves seen in [18] is because we have mapped our waveform to the super rest frame using supertranslations, rather than changing the waveform by a constant. While the two actions have similar effects, supertranslations also affect the coordinates, which is not true of changing the waveform by a constant. This is illustrated by the red curve in the bottom right plot of Figs. 6, 7, and 8. Therefore, Fig. 9 clearly illustrates the importance of mapping to the super rest frame, even for modes such as the $(2, 2)$ mode where such effects were thought to be negligible.

Based on the results that are shown in Fig. 6, one's immediate response to this issue of BMS frames might be to simply fit the QNM model to the news instead of the strain, seeing as the displacement memory effect is not present in the news. To counter this proposal, however, we provide Fig. 10, which shows the mismatch between numerical waveforms and QNM models built from 100 modes for a wide range of systems whose parameters can be found in Table I. In the top panel, we are performing our QNM fits in the strain domain, while in the bottom panel we are performing our QNM fits in the news domain. For each panel, we also show four types of mismatch comparison: when the numerical waveforms are extrapolated waveforms (EXT) and when the CCE waveforms (i) are not mapped to a certain BMS frame; (ii) have been mapped to just the center-of-mass (CoM) frame, or (iii) have been mapped to the the super rest frame using the procedures outlined in [33]. As can be seen in the
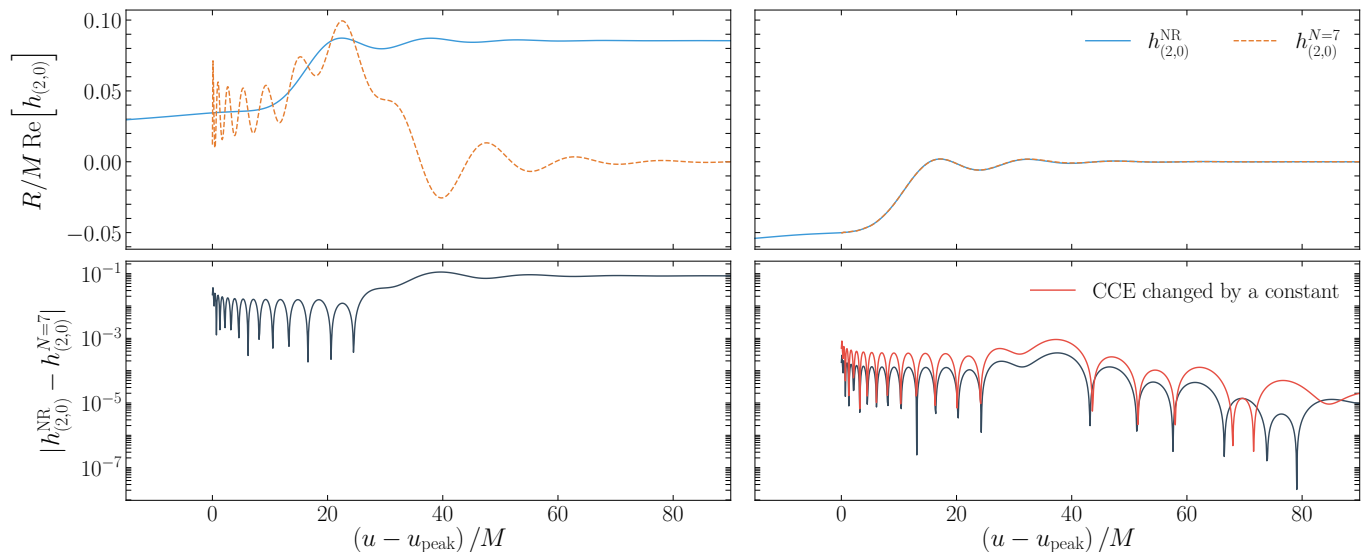
FIG. 6. Comparison between the real component of the $(2,0)$ mode of a CCE waveform and the QNM model built from the $(2,0)$ mode with $n = 0$ and 7 overtones. The upper panels show both waveforms, while the lower panels show the residual between the two. In the plots on the left, we are using a NR waveform in the center-of-mass frame of the remnant BH, while in the plots on the right we have mapped the NR waveform to the super rest frame using the method outlined in Sec. II and Appendix A of [33]. In the bottom right plot, we also show a residual curve in red, whose NR waveform has been mapped to the center-of-mass frame of the remnant BH and changed by a constant so that it obtains a final value of zero. We include this curve to illustrate that by performing a supertranslation, rather than changing the strain by a constant, one can obtain much more accurate QNM fits due to the mode-mixing that is induced by supertranslations [36].
BBH merger: `SXS:BBH:0305`.
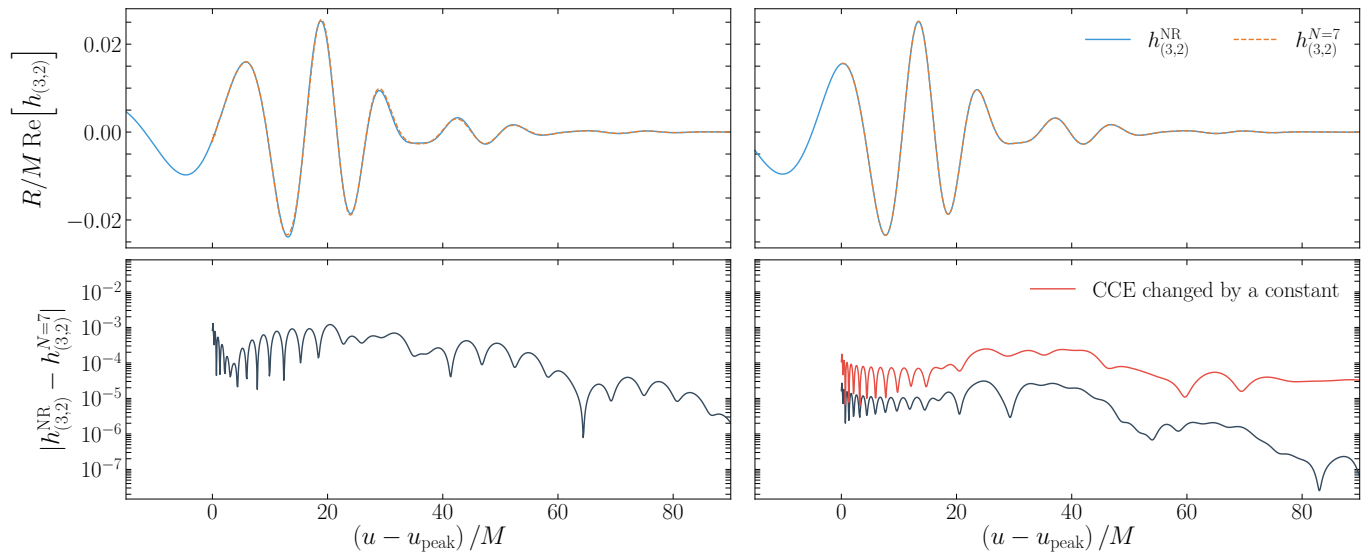
FIG. 7. The same as Fig. 6, but for the $(3,2)$ mode. Note that when building this QNM model we have included not only the $(3, 2, 0 - 7)$ modes, but also the $(2, 2, 0 - 7)$ modes because these modes are needed to accurately represent the $(3,2)$ mode due to the spherical-spheroidal mixing that occurs when changing the basis of the QNM model.

top panel, mapping to the super rest frame, on average, improves the mismatches by 5 orders of magnitude. This, however, should not come as a surprise seeing as this result is predominantly due to supertranslating away the offset in the strain induced by the gravitational memory effect, e.g., what is shown in Fig. 6. What might be surprising is

what is shown in the bottom panel: namely that mapping to the super rest frame, on average, also improves the mismatches in the news domain by a factor of 4. Due to this, we now realize that mapping to the super rest frame is even important in the news or Ψ_4 domains where there is no memory effect. This phenomenon is due to the mode
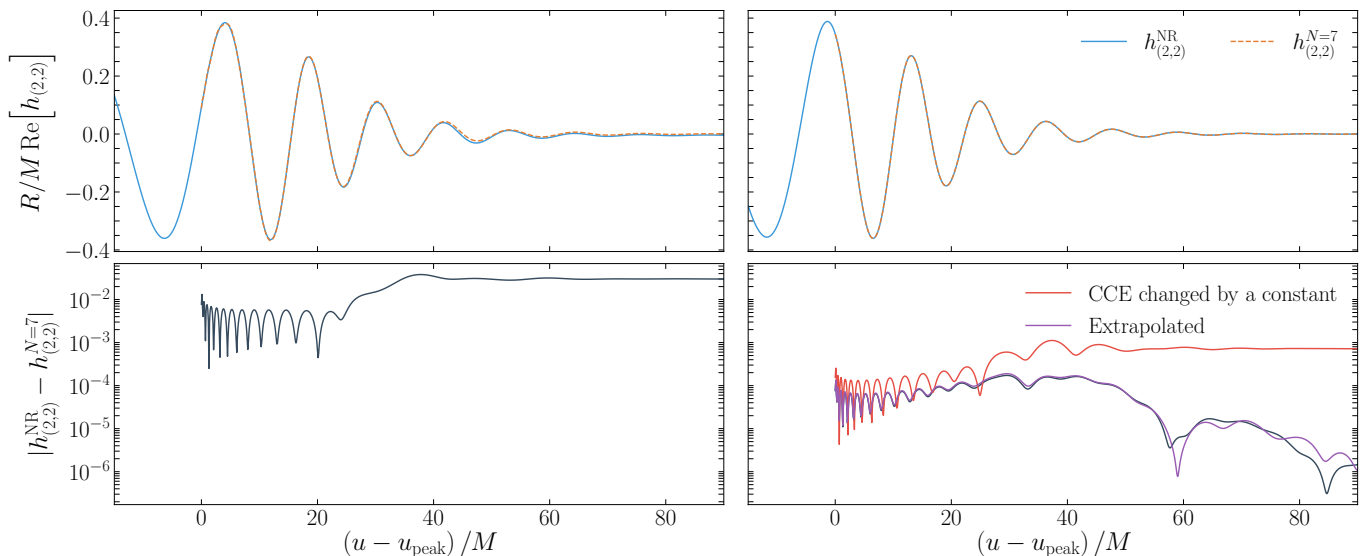
FIG. 8. The same as Fig. 6, but for the (2,2) mode. We also include the purple curve, which illustrates the previous result obtained by [23, 25] when using an extrapolated waveform which has been changed by a constant so that its final value is zero.
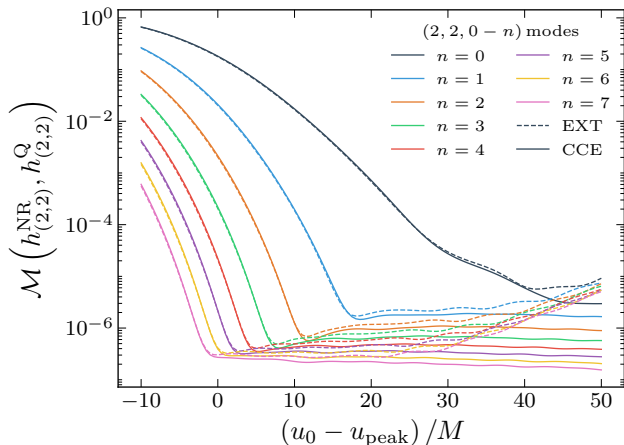

FIG. 9. Comparing the mismatch curves for the $(2, 2)$ mode and its overtones obtained from the extrapolated waveform used in [18] and [19] (dashed curves) as well as the corresponding CCE waveform, after it was mapped to the super rest frame (solid curves). This plot also serves the purpose of clarifying why Fig. 1 of [18] and Fig. 2 of [19] are different. In [18], they performed an ad hoc subtraction of their waveform, while in [19] no such change to the extrapolated waveform was performed. Note that for this plot we only include the prograde modes in our QNM model to remain consistent with the results of [18] and [19]. BBH merger: `SXS:BBH:0305`.

mixing that occurs due to the change in coordinates of the system by the supertranslations.

Last, to help illustrate what brings about these changes in the mismatch as a function of frame, we present Fig. 11. In Fig. 11 we show how the fraction of unmodeled power varies as a function of mode for strain and news waveforms

in the center-of-mass or super rest frame for the simulation `SXS:BBH:0305`. More specifically, for each waveform we build a QNM model using every available mode and then we compute the fraction of unmodeled power between the numerical waveform and the QNM model using Eq. (29) (top plot) or Eq. (30) (bottom plot) with the residual, i.e., Eq. (26) or Eq. (27), only involving the corresponding mode of the waveform and the QNM model. We organize the modes in terms of the largest relative difference in the fraction of unmodeled power in the strain domain between the center-of-mass and the super rest frame waveforms. As can be seen, in the strain domain the modes that are most strongly impacted by the super rest frame are the $(2, \pm2)$ modes, the $(3, \pm2)$ modes, and the $m = 0$ modes. This occurs for many reasons. For the $m = 0$ modes, this is most naturally understood by realizing that these modes often exhibit more memory effects than others and thus require the supertranslations to reduce the offset normally found in the ringdown phase of these modes. Put differently, these modes are strongly influenced by the $\bar{\eth}^2 \alpha(\theta, \phi)$ factor in Eq. (11). For the $(3, \pm2)$ modes, the reason why these modes are impacted is because of the mode-mixing that occurs due to Taylor expanding the strain in the supertranslated coordinate system about the original coordinate system. For the supertranslations that we apply to map to the super rest frame, the most dominant mode is the $(2, 0)$ mode. Consequently, since the dominant modes of the news are the $(2, \pm2)$ modes, the mode of the new strain that will be most influenced by the supertranslation's mode mixing is the mode corresponding to the product of the $Y_{(2,0)}$ and $_{-2}Y_{(2,\pm2)}$ functions, which happens to be the $(3, \pm2)$ mode. This can be seen directly by making use of the spin-weighted spherical harmonic triple integral identity:
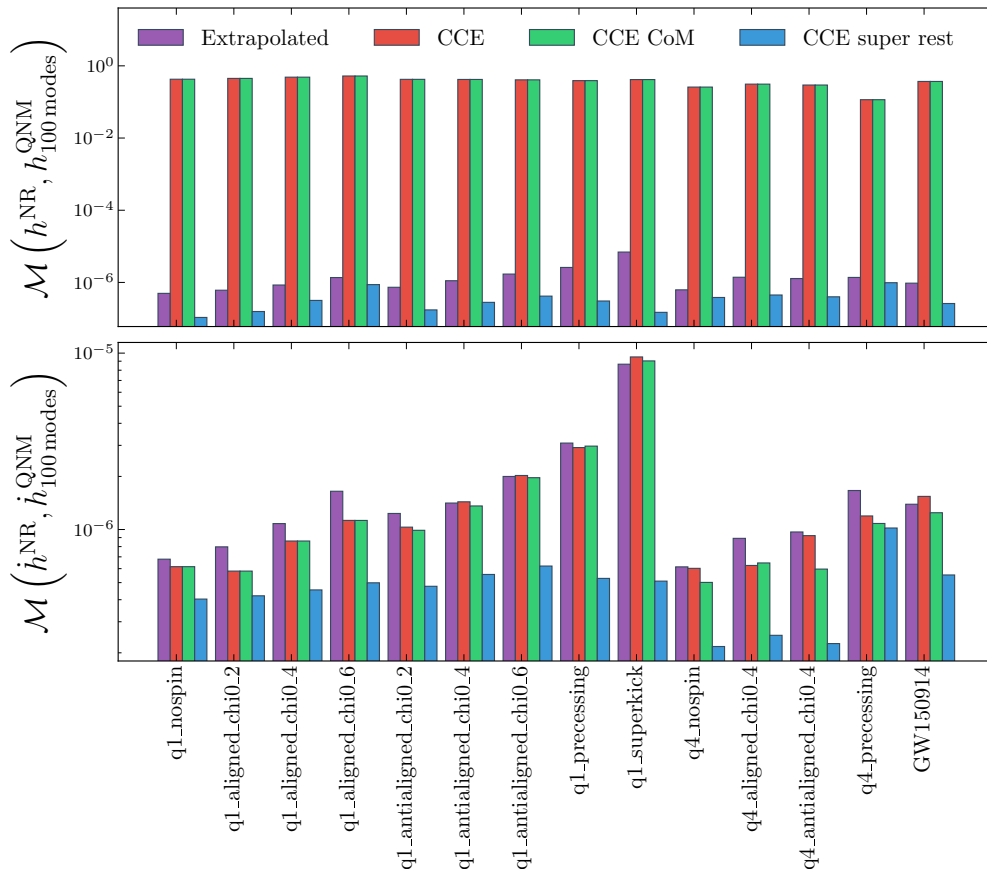
FIG. 10. Examining the mismatch between a NR waveform and a QNM model that is built from 100 modes as a function of the BMS frame that the numerical waveform is mapped to. The QNM model start time u_0 is taken to be the time at which the L^2 norm of the news takes on its maximum value. We show four bars that correspond to the extrapolated waveform (EXT) and the CCE waveform in three different BMS frames: the arbitrary BMS frame that the output of CCE is in, the remnant BH's center-of-mass frame, and the super rest frame. In the top plot, we show the mismatch between the strain waveforms, while in the bottom plot we show the mismatch between the news waveforms. The parameters of the 14 binary black holes mergers that appear on the horizontal axis can be found in Table I.

$$\int_{S^2} {}_{s_1}Y_{\ell_1 m_1}\,{}_{s_2}Y_{\ell_2 m_2}\,{}_{s_3}Y_{\ell_3 m_3} = \sqrt{\frac{(2\ell_1+1)(2\ell_2+1)(2\ell_3+1)}{4\pi}} \begin{pmatrix} \ell_1 & \ell_2 & \ell_3 \\ m_1 & m_2 & m_3 \end{pmatrix} \begin{pmatrix} \ell_1 & \ell_2 & \ell_3 \\ -s_1 & -s_2 & -s_3 \end{pmatrix} \tag{32}$$

for $s_1 + s_2 + s_3 = 0$, and then computing the corresponding Wigner $3 - j$ symbols to see which modes are excited [77]. Last, for the $(2, \pm 2)$ modes, this is because these two modes of the strain experience an unexpected initial offset due to transient effects arising in the CCE evolution [50, 64, 65]. Meanwhile, in the news domain, by closer inspection one finds that the modes most strongly influenced by mapping to the super rest frame are the $(3, \pm 2)$, $(4, \pm 2)$, and $(2, \pm 1)$ modes. Like the case of the $(3, \pm 2)$ modes in the strain domain, this is because these modes also experience considerable changes due to super-translation mode-mixing effects, as can be verified with Eq. (32). The other important thing to note regarding Fig. 11, as well as Fig. 10, is that by mapping CCE wave-

forms to the super rest frame, we can always produce a better mismatch between the numerical waveform and the QNM model than if we were using an extrapolated waveform.

V. CONCLUSION

Across this study, we have developed a QNM model which simultaneously fits multiple modes over all angles and times using NR waveforms that have been mapped to the super rest frame. First, we showed that for SXS:BBH:0305 the amount of power captured in the QNM model when fitting to only the dominant strain $(2, \pm 2)$
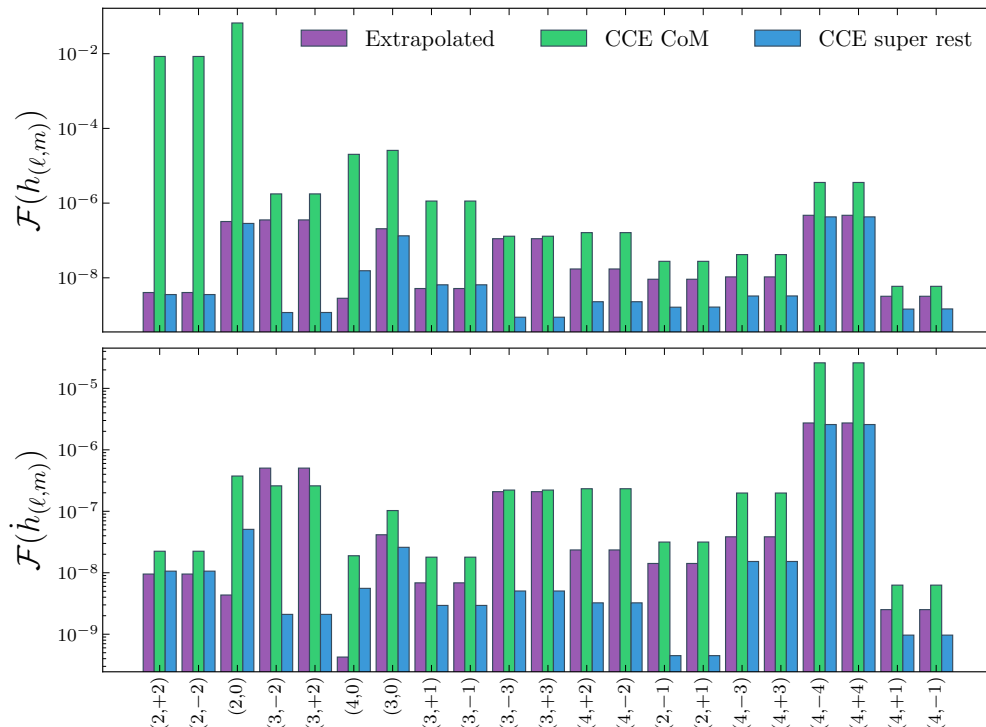
FIG. 11. Examining the fraction of unmodeled power between a NR waveform and a QNM model that n is built from 168 modes as a function of mode for extrapolated (EXT) and CCE waveforms. The QNM model start time u_0 is taken to be u_{peak}. We show three bars that correspond to the extrapolated waveform, the CCE waveform in the remnant BH's center-of-mass frame, and the CCE waveform in super rest frame. In the top plot, we show the fraction of unmodeled power between the strain waveforms, while in the bottom plot we show the fraction of unmodeled power between the news waveforms. The modes are organized in terms of the largest relative difference in the fraction of unmodeled power in the strain domain between the center-of-mass and super rest frame CCE waveforms.

BBH merger: `SXS:BBH:0305`.

modes is below 65% of the whole numerical waveform's power over all modes. Moreover, we also found that including the $(2, \pm 2)$ overtone modes does not dramatically increase the power modeled, except at times very close to $u_0 = u_{\text{peak}}$, in which case a 50% improvement over the fundamental mode can be seen by including 7 overtones. To increase the amount of modeled power, one must instead rely on higher-order modes.

Choosing which higher-order modes to include in the QNM model is a nontrivial task. Therefore, we developed a greedy algorithm that picks which modes to include based on the fraction of unmodeled power in them. We find that by including just 5 modes, we can model 96% of a waveform's power and by including just 20 modes, we can push that number up to 99%. We also find an all-angles mismatch improvement by a factor of 10^5 when using multimode fitting as compared to using the $(2, \pm 2, n)$ modes. Furthermore, we also showed the practical importance of this higher-order mode power modeling improvement: obtaining more accurate estimates of the remnant's mass and spin. With 40 modes we found that we can, on average, obtain mass and spin estimates that yield an epsilon value (see Eq. (31)) that is more than half an order of

magnitude better than what can be obtained by using the $(2, 2)$ mode with 7 overtones. While we found that we can further improve estimates by including even more modes, the minimum median epsilon that we computed was only 62% less than that obtained by using 40 modes. We attribute this to the fact that by including higher-order modes, there are more nonlinearities that the QNM model has to try and fit (see, e.g., Fig. 2 of [50]).[6]

Greedy algorithms can suffer instabilities due to degeneracy in the underlying model [78]. However, we know that the overlaps between different QNM modes with distinct angular indices (ℓ, m) are small for the spins that we are considering because the angular part of the QNM (l, m, n, p) is dominantly in the (l, m) spherical harmonic. Therefore, any degeneracy we might expect is likely only due to the overtone number [22]. Since the overtones are chosen sequentially, and not greedily, our algorithm should not suffer from such degeneracy problems. Never-

---

[6] In Fig. 2 of [50] the blue and green curves in the middle plot represent nonlinearities, which would not be captured by the QNM model.

theless, this is an important check to keep in mind and would be interesting to examine in the future.

Lastly, we also illustrated the importance of using waveforms that have been mapped to the same BMS frame as that of the QNM model. As shown in Figs. 6, 7, 8, 9, 10, and 11 if one does not map their waveforms to the super rest frame then being in the wrong BMS frame makes it problematic to model the ringdown part of a waveform with QNMs. This is because when the Teukolsky equation is separated, the coordinate system used corresponds to the super rest frame at $\mathscr{I}^+$. Thus the QNM ansatz in Eq. (4) is only valid in this frame. On the other hand, numerical simulations have a history of radiated gravitational waves that cause their frame to typically deviate significantly from this frame. Consequently, the waveforms emitted by these ringing black holes need to be mapped to the super rest frame, if they are to be correctly modeled by QNMs. Furthermore, this importance of BMS frames extends beyond accounting for the memory effect in the strain. In Fig. 10, we showed that while mapping to the super rest frame is most important for modeling the strain, it also plays a nontrivial role in modeling the news because supertranslations also change the Bondi coordinates and can thus reduce supertranslation-induced mode-mixing in the news. Overall, we found that previous studies that focus on modeling the $(2, 2)$ mode from extrapolated waveforms are only slightly impacted by mapping to the super rest frame. However, with the inclusion of more modes or memory effects, fixing the BMS frame before fitting QNMs is crucial.

As is illustrated by the fact that future ground-based detectors like the Einstein Telescope and Cosmic Explorer are expected to observe $10^2 - 10^4$ events per year with strong ringdown signals, including higher-order modes and BMS frame fixing will undoubtedly be important for correctly modeling such ringdown signals with QNMs. These modeling enhancements should therefore also help with measuring properties of the remnant black holes as well as testing Einstein's theory of relativity [27, 28, 79]. While BMS frame fixing may not prove to be directly useful for LIGO/Virgo observations,[7] if the ringdown phase of NR waveforms is to be used to study remnant BHs and model their amplitudes then fixing the BMS frame will certainly be important, as illustrated in this work. Furthermore, while we have presented a template for improving QNM models by comparing QNMs against numerical relativity waveforms, it would be very interesting to see our work applied to the observations already collected by LIGO and Virgo.

---

[7] Because the detector measures the waveform at a single point on the sky only, the supertranslation will only shift the waveform.

REFERENCES

[1] L. Barack, V. Cardoso, S. Nissanke, T. P. Sotiriou, A. Askar, C. Belczynski, G. Bertone, E. Bon, D. Blas, R. Brito, and et al., Black holes, gravitational waves and fundamental physics: a roadmap, Classical and Quantum Gravity **36**, 143001 (2019).

[2] B. P. Abbott et al. (LIGO Scientific, Virgo), Observation of Gravitational Waves from a Binary Black Hole Merger, Phys. Rev. Lett. **116**, 061102 (2016), arXiv:1602.03837 [gr-qc].

[3] B. P. Abbott et al. (LIGO Scientific, Virgo), GW170817: Observation of Gravitational Waves from a Binary Neutron Star Inspiral, Phys. Rev. Lett. **119**, 161101 (2017), arXiv:1710.05832 [gr-qc].

[4] R. Abbott et al. (LIGO Scientific, VIRGO, KAGRA), GWTC-3: Compact Binary Coalescences Observed by LIGO and Virgo During the Second Part of the Third Observing Run, arXiv:2111.03606 [gr-qc].

[5] R. Abbott et al. (LIGO Scientific, VIRGO, KAGRA), Tests of General Relativity with GWTC-3, arXiv:2112.06861 [gr-qc].

[6] F. Pretorius, Evolution of binary black hole spacetimes, Phys. Rev. Lett. **95**, 121101 (2005), arXiv:gr-qc/0507014.

[7] M. Boyle et al., The SXS Collaboration catalog of binary black hole simulations, Class. Quant. Grav. **36**, 195006 (2019), arXiv:1904.04831 [gr-qc].

[8] K. Jani, J. Healy, J. A. Clark, L. London, P. Laguna, and D. Shoemaker, Georgia tech catalog of gravitational

waveforms, Classical and Quantum Gravity **33**, 204001 (2016).

[9] J. Healy, C. O. Lousto, Y. Zlochower, and M. Campanelli, The rit binary black hole simulations catalog, Classical and Quantum Gravity **34**, 224001 (2017).

[10] J. Healy and C. O. Lousto, Third rit binary black hole simulations catalog, Phys. Rev. D **102**, 104018 (2020), arXiv:2007.07910 [gr-qc].

[11] S. A. Teukolsky, Perturbations of a Rotating Black Hole. I. Fundamental Equations for Gravitational, Electromagnetic, and Neutrino-Field Perturbations, Astrophys. J. **185**, 635 (1973).

[12] S. L. Detweiler, Black Holes and Gravitational Waves. III. The Resonant Frequencies of Rotating Holes, Astrophys. J. **239**, 292 (1980).

[13] E. W. Leaver, An Analytic representation for the quasi normal modes of Kerr black holes, Proc. Roy. Soc. Lond. A **402**, 285 (1985).

[14] S. R. Dolan and A. C. Ottewill, On an Expansion Method for Black Hole Quasinormal Modes and Regge Poles, Class. Quant. Grav. **26**, 225003 (2009), arXiv:0908.0329 [gr-qc].

[15] G. B. Cook and M. Zalutskiy, Gravitational perturbations of the Kerr geometry: High-accuracy study, Phys. Rev. D **90**, 124021 (2014), arXiv:1410.7698 [gr-qc].

[16] M. Isi and W. M. Farr, Analyzing black-hole ringdowns, arXiv:2107.05609 [gr-qc].

[17] W. H. Press and S. A. Teukolsky, Perturbations of a Rotating Black Hole. II. Dynamical Stability of the Kerr Metric, Astrophys. J. **185**, 649 (1973).

[18] M. Giesler, M. Isi, M. A. Scheel, and S. Teukolsky, Black Hole Ringdown: The Importance of Overtones, Phys. Rev. X **9**, 041060 (2019), arXiv:1903.08284 [gr-qc].

[19] G. B. Cook, Aspects of multimode Kerr ringdown fitting, Phys. Rev. D **102**, 024027 (2020), arXiv:2004.08347 [gr-qc].

[20] L. London, D. Shoemaker, and J. Healy, Modeling ringdown: Beyond the fundamental quasinormal modes, Phys. Rev. D **90**, 124032 (2014), [Erratum: Phys.Rev.D 94, 069902 (2016)], arXiv:1404.3197 [gr-qc].

[21] V. Baibhav and E. Berti, Multimode black hole spectroscopy, Phys. Rev. D **99**, 024005 (2019), arXiv:1809.03500 [gr-qc].

[22] E. Berti and A. Klein, Mixing of spherical and spheroidal modes in perturbed Kerr black holes, Phys. Rev. D **90**, 064012 (2014), arXiv:1408.1860 [gr-qc].

[23] A. Dhani and B. S. Sathyaprakash, Overtones, mirror modes, and mode-mixing in binary black hole mergers, arXiv:2107.14195 [gr-qc].

[24] E. Finch and C. J. Moore, Modeling the ringdown from precessing black hole binaries, Phys. Rev. D **103**, 084048 (2021), arXiv:2102.07794 [gr-qc].

[25] A. Dhani, Importance of mirror modes in binary black hole ringdown waveform, Phys. Rev. D **103**, 104048 (2021), arXiv:2010.08602 [gr-qc].

[26] X. Li, L. Sun, R. K. L. Lo, E. Payne, and Y. Chen, Angular emission patterns of remnant black holes, Phys. Rev. D **105**, 024016 (2022), arXiv:2110.03116 [gr-qc].

[27] M. Maggiore *et al.*, Science Case for the Einstein Telescope, JCAP **03**, 050, arXiv:1912.02622 [astro-ph.CO].

[28] V. Baibhav, E. Berti, D. Gerosa, M. Mapelli, N. Giacobbo, Y. Bouffanais, and U. N. Di Carlo, Gravitational-wave detection rates for compact binaries formed in isolation: LIGO/Virgo O3 and beyond, Phys. Rev. D **100**, 064060 (2019), arXiv:1906.04197 [gr-qc].

[29] E. Berti, V. Cardoso, and C. M. Will, On gravitational-wave spectroscopy of massive black holes with the space interferometer LISA, Phys. Rev. D **73**, 064030 (2006), arXiv:gr-qc/0512160.

[30] E. Barausse *et al.*, Prospects for Fundamental Physics with LISA, Gen. Rel. Grav. **52**, 81 (2020), arXiv:2001.09793 [gr-qc].

[31] J. Bellovary *et al.* (NASA LISA Study Team), Getting Ready for LISA: The Data, Support and Preparation Needed to Maximize US Participation in Space-Based Gravitational Wave Science, arXiv:2012.02650 [astro-ph.IM].

[32] C. J. Woodford, M. Boyle, and H. P. Pfeiffer, Compact Binary Waveform Center-of-Mass Corrections, Phys. Rev. D **100**, 124010 (2019), arXiv:1904.04842 [gr-qc].

[33] K. Mitman *et al.*, Fixing the BMS frame of numerical relativity waveforms, Phys. Rev. D **104**, 024051 (2021), arXiv:2105.02300 [gr-qc].

[34] H. Bondi, M. G. J. Van der Burg, and A. W. K. Metzner, Gravitational waves in general relativity, VII. Waves from axi-symmetric isolated system, Proceedings of the Royal Society of London. Series A. Mathematical and Physical Sciences **269**, 21 (1962).

[35] R. K. Sachs and H. Bondi, Gravitational waves in general relativity VIII. Waves in asymptotically flat space-time, Proceedings of the Royal Society of London. Series A. Mathematical and Physical Sciences **270**, 103 (1962).

[36] M. Boyle, Transformations of asymptotic gravitational-wave data, Phys. Rev. D **93**, 084031 (2016), arXiv:1509.00862 [gr-qc].

[37] O. M. Moreschi, Supercenter of Mass System at Future Null Infinity, Class. Quant. Grav. **5**, 423 (1988).

[38] O. M. Moreschi and S. Dain, Rest frame system for asymptotically flat space-times, J. Math. Phys. **39**, 6631 (1998), arXiv:gr-qc/0203075.

[39] S. Dain and O. M. Moreschi, General existence proof for rest frame systems in asymptotically flat space-time, Class. Quant. Grav. **17**, 3663 (2000), arXiv:gr-qc/0203048.

[40] H. Lim, G. Khanna, A. Apte, and S. A. Hughes, Exciting black hole modes via misaligned coalescences: II. The mode content of late-time coalescence waveforms, Phys. Rev. D **100**, 084032 (2019), arXiv:1901.05902 [gr-qc].

[41] L. C. Stein, qnm: A Python package for calculating Kerr quasinormal modes, separation constants, and spherical-spheroidal mixing coefficients, J. Open Source Softw. **4**, 1683 (2019), arXiv:1908.10377 [gr-qc].

[42] J. N. Goldberg, A. J. MacFarlane, E. T. Newman, F. Rohrlich, and E. C. G. Sudarshan, Spin s spherical harmonics and edth, J. Math. Phys. **8**, 2155 (1967).

[43] E. T. Newman and R. Penrose, Note on the Bondi-Metzner-Sachs group, J. Math. Phys. **7**, 863 (1966).

[44] L. London and E. Fauchon-Jones, On modeling for Kerr black holes: Basis learning, QNM frequencies, and spherical-spheroidal mixing coefficients, Class. Quant. Grav. **36**, 235015 (2019), arXiv:1810.03550 [gr-qc].

[45] M. Boyle, How should spin-weighted spherical functions be defined?, J. Math. Phys. **57**, 092504 (2016), arXiv:1604.08140 [gr-qc].

[46] Y. B. Zel'dovich and A. G. Polnarev, Radiation of gravitational waves by a cluster of superdense stars, Sov. Astron. **18**, 17 (1974).

[47] V. B. Braginsky and K. S. Thorne, Gravitational-wave bursts with memory and experimental prospects, Nature **327**, 123 (1987).

[48] D. Christodoulou, Nonlinear nature of gravitation and gravitational-wave experiments, Phys. Rev. Lett. **67**, 1486 (1991).

[49] K. S. Thorne, Gravitational-wave bursts with memory: The christodoulou effect, Phys. Rev. D **45**, 520 (1992).

[50] K. Mitman, J. Moxon, M. A. Scheel, S. A. Teukolsky, M. Boyle, N. Deppe, L. E. Kidder, and W. Throwe, Computation of displacement and spin gravitational memory in numerical relativity, Phys. Rev. D **102**, 104007 (2020), arXiv:2007.11562 [gr-qc].

[51] A. M. Grant and D. A. Nichols, Persistent gravitational wave observables: Curve deviation in asymptotically flat spacetimes, arXiv:2109.03832 [gr-qc].

[52] R. Geroch, A. Held, and R. Penrose, A space-time calculus based on pairs of null directions, J. Math. Phys. **14**, 874 (1973).

[53] E. E. Flanagan and D. A. Nichols, Conserved charges of the extended Bondi-Metzner-Sachs algebra, Phys. Rev. D **95**, 044002 (2017), arXiv:1510.03386 [hep-th].

[54] D. A. B. Iozzo, M. Boyle, N. Deppe, J. Moxon, M. A. Scheel, L. E. Kidder, H. P. Pfeiffer, and S. A. Teukolsky, Extending gravitational wave extraction using weyl characteristic fields, Phys. Rev. D **103** (2021), arXiv:2010.15200 [gr-qc].

[55] O. M. Moreschi, On angular momentum at future null infinity, Class. Quantum Gravity **3**, 503 (1986).

[56] C. R. Harris *et al.*, Array programming with NumPy, Nature **585**, 357 (2020), arXiv:2006.10256 [cs.MS].

[57] P. Virtanen *et al.*, SciPy 1.0–Fundamental Algorithms for Scientific Computing in Python, Nature Meth. **17**, 261 (2020), arXiv:1907.10121 [cs.MS].

[58] F. Gao and L. Han, Implementing the nelder-mead simplex algorithm with adaptive parameters, Computational Optimization and Applications **51**, 259 (2012).

[59] D. A. B. Iozzo *et al.*, Comparing Remnant Properties from Horizon Data and Asymptotic Data in Numerical Relativity, Phys. Rev. D **103**, 124029 (2021), arXiv:2104.07052 [gr-qc].

[60] SXS Ext-CCE Waveform Database, `https://data.black-holes.org/waveforms/extcce_catalog.html`.

[61] SXS Gravitational Waveform Database, `http://www.black-holes.org/waveforms`.

[62] `https://www.black-holes.org/code/SpEC.html`.

[63] D. A. B. Iozzo, M. Boyle, N. Deppe, J. Moxon, M. A. Scheel, L. E. Kidder, H. P. Pfeiffer, and S. A. Teukolsky, Extending gravitational wave extraction using Weyl characteristic fields, Phys. Rev. D **103**, 024039 (2021), arXiv:2010.15200 [gr-qc].

[64] J. Moxon, M. A. Scheel, and S. A. Teukolsky, Improved Cauchy-characteristic evolution system for high-precision numerical relativity waveforms, Phys. Rev. D **102**, 044052 (2020), arXiv:2007.01339 [gr-qc].

[65] J. Moxon, M. A. Scheel, S. A. Teukolsky, N. Deppe, N. Fischer, F. Hébert, L. E. Kidder, and W. Throwe, The SpECTRE Cauchy-characteristic evolution system for rapid, precise waveform extraction, arXiv:2110.08635 [gr-qc].

[66] M. Boyle, D. Iozzo, and L. C. Stein, moble/scri: v1.2 (2020).

[67] M. Boyle, Angular velocity of gravitational radiation from precessing binaries and the corotating frame, Phys. Rev. D **87**, 104006 (2013), arXiv:1302.2919 [gr-qc].

[68] M. Boyle, L. E. Kidder, S. Ossokine, and H. P. Pfeiffer, Gravitational-wave modes from precessing black-hole binaries, arXiv:1409.4431 [gr-qc].

[69] N. Deppe, W. Throwe, L. E. Kidder, N. L. Fischer, C. Armaza, G. S. Bonilla, F. Hébert, P. Kumar, G. Lovelace, J. Moxon, E. O'Shea, H. P. Pfeiffer, M. A. Scheel, S. A. Teukolsky, I. Anantpurkar, M. Boyle, F. Foucart, M. Giesler, D. A. B. Iozzo, I. Legred, D. Li, A. Macedo, D. Melchor, M. Morales, T. Ramirez, H. R. Rüter, J. Sanchez, S. Thomas, and T. Wlodarczyk, SpECTRE (2020).

[70] K. Mitman *et al.*, Adding gravitational memory to waveform catalogs using BMS balance laws, Phys. Rev. D **103**, 024031 (2021), arXiv:2011.01309 [gr-qc].

[71] O. Sarbach and M. Tiglio, Gauge invariant perturbations of Schwarzschild black holes in horizon penetrating coordinates, Phys. Rev. D **64**, 084016 (2001), arXiv:gr-qc/0104061.

[72] T. Regge and J. A. Wheeler, Stability of a Schwarzschild singularity, Phys. Rev. **108**, 1063 (1957).

[73] F. J. Zerilli, Effective potential for even parity Regge-Wheeler gravitational perturbation equations, Phys. Rev. Lett. **24**, 737 (1970).

[74] M. Boyle and A. H. Mroue, Extrapolating gravitational-wave data from numerical simulations, Phys. Rev. D **80**, 124045 (2009), arXiv:0905.3177 [gr-qc].

[75] X. J. Forteza and P. Mourier, High-overtone fits to numerical relativity ringdowns: beyond the dismissed n=8 special tone, arXiv:2107.11829 [gr-qc].

[76] V. Varma, S. E. Field, M. A. Scheel, J. Blackman, L. E. Kidder, and H. P. Pfeiffer, Surrogate model of hybridized numerical relativity binary black hole waveforms, Phys. Rev. D **99**, 064045 (2019), arXiv:1812.07865 [gr-qc].

[77] W. B. Campbell and T. Morgan, Debye Potentials for the Gravitational Field, Physica **53**, 264 (1971).

[78] I. Guyon and A. Elisseeff, An introduction to variable and feature selection, J. Mach. Learn. Res. **3**, 1157 (2003).

[79] M. Isi, M. Giesler, W. M. Farr, M. A. Scheel, and S. A. Teukolsky, Testing the no-hair theorem with GW150914, Phys. Rev. Lett. **123**, 111102 (2019), arXiv:1905.00869 [gr-qc].

[80] J. D. Hunter, Matplotlib: A 2D Graphics Environment, Comput. Sci. Eng. **9**, 90 (2007).